Modelling the variable emission states of γ-ray-emitting narrow-line Seyfert 1 galaxies

Anna Luashvili [ORCID],[1][⋆] Catherine Boisson,[1][⋆] Andreas Zech [ORCID],[1][⋆] Maialen Arrieta-Lobo[2] and Daniel Kynoch [ORCID][3]

[1]*Laboratoire Univers et Théories, Observatoire de Paris, Université PSL, Université Paris Cité, CNRS, F-92190 Meudon, France*
[2]*Sorbonne Université, Centre National de la Recherche Scientifique UMR 8256, Paris, France*
[3]*School of Physics and Astronomy, University of Southampton, University Road, Southampton, SO17 1BJ, UK*

ABSTRACT

γ-ray-emitting narrow-line Seyfert 1 galaxies (γ-NLS1) constitute an intriguing small population of active galactic nuclei with γ-ray emission resembling low-power flat-spectrum radio quasars (FSRQ), but with differing physical properties. They are jetted, γ/radio-loud Seyfert galaxies, with relatively low black hole masses, accreting at exceptionally high, near-Eddington rates. Certain of these sources exhibit highly variable emission states on relatively short time-scales, the physical origin of which remains elusive. In this work, varying emission states of two bona fide NLS1s, 1H 0323+342 and PMN J0948+0022, and one little-studied FSRQ/intermediate object, B2 0954+25A, are examined. For each source, we analysed quasi-simultaneous multiwavelength data for different states of γ-ray activity and present the results of their broad-band emission modelling, taking into account all available physical constraints to limit the range of the model parameters. Two different scenarios are discussed, in the framework of a one-zone leptonic model, where the high-energy emission is due to the inverse Compton scattering of the disc and broad line region (BLR) or torus photons by relativistic electrons within the jet. The transition from low to high state is well described by variations of the jet parameters, leaving the external photon fields unchanged. The parameterization favours an emission scenario with particle injection on a stationary shock inside the jet. When considering all physical constraints, the disc and BLR scenario is preferred for all three sources. We use the multi-epoch modelling to characterize total jet powers and discuss the intrinsic nature of γ-NLS1 galaxies and FSRQs.

Key words: galaxies: active – gamma-rays: galaxies – galaxies: Seyfert – galaxies: jets – galaxies: individual: 1H 0323+342 – galaxies: individual: PMN J0948+0022 – galaxies: individual: B2 0954+25A.

1 INTRODUCTION

Since their identification as a particular class of broad-line active galactic nuclei (AGNs), narrow-line Seyfert 1 galaxies (NLS1s) have drawn substantial attention. NLS1s share some optical features with typical broad-line Seyfert 1s, but have narrower permitted emission lines (FWHM (Hβ) $< 2000 \, \mathrm{kms^{-1}}$), pointing to a relatively low-mass black hole (BH) ($\sim 10^6 - 10^8 M_\odot$), fairly intense FeII and OI emission, and weak [O III] lines with a ratio [O III] to Hβ < 3 (Osterbrock & Pogge 1985; Goodrich 1989). In the X-rays, NLS1s also have extreme properties such as a remarkably soft X-ray excess ($0.5 - 2$ keV) or rapid and large-amplitude observed variability (Boller, Brandt & Fink 1996). These X-ray characteristics that set NLS1s apart from other Seyfert types are mainly due to their high Eddington accretion rates ($L/L_{\rm Edd} \sim 0.1 - 10$, Boroson & Green 1992; Boller et al. 1996) and their low-mass BHs with regards to Seyfert 1s. NLS1s are mostly radio-quiet, like Seyfert 1s, although a small fraction, ~ 4–7 per cent, has been found to be radio-loud with a flat radio spectrum (see e.g. Komossa et al. 2006; Rakshit et al. 2017).

The detection of a small fraction of the radio-loud NLS1 galaxies by the *Fermi* Gamma-Ray Space Telescope (Abdo et al. 2009a) has led to a new γ-loud class of AGNs that joins the well-known γ-ray-emitting radio galaxies and blazars. Due to their low BH masses compared to blazars, NLS1s were not expected to harbour relativistic jets that could create such high-energy emission. The fact that this new type of γ-loud AGN features both blazar- and Seyfert-like characteristics could bring us closer to a better understanding of AGN unification, beyond the effect of their jet orientation, to describe different AGN types and provide new insight into the physics of the formation and evolution of radio jets under high accretion-rate conditions. About 20 objects of this class have now been reported in the high-energy (HE) band with *Fermi*-LAT; eight of them are listed in the fourth Fermi-LAT source catalogue (4FGL; Abdollahi et al. 2020) (see Paliya et al. 2019; Foschini 2020 for a recent review). They present both similarities and differences with the more powerful jetted AGNs, notably flat-spectrum radio quasar (FSRQs), see e.g. Foschini (2020) and D'Ammando (2019).

Studies investigating the intrinsic power of relativistic jets in γ-NLS1s, and comparing them with the blazar class (e.g. Foschini et al. 2015; Paliya et al. 2019), are not easily comparable to each other, since they are based on different assumptions and methods, making it difficult to draw clear conclusions.

⋆ E-mail: anna.luashvili@obspm.fr (AL); catherine.boisson@obspm.fr (CB); andreas.zech@obspm.fr (AZ)

The evidence of γ-ray emission poses the question of the location of the γ-ray emitting zone and the contribution of the γ-γ absorption within the broad line region (BLR), since such objects are detected by *Fermi*-LAT but not by existing imaging Cherenkov telescopes, which have typical energy thresholds of at least a few 10 GeV. Some of the γ-NLS1s show strongly changing spectral properties, in some cases even switching between Seyfert-type (accretion disc-dominated) to blazar type (completely jet-dominated) states (e.g. D'Ammando et al. 2015). A better understanding of the mechanism behind varying emission states might be a key to constrain the overall emission process and the location of the emission region. Hence, detailed studies involving multi-epoch spectral energy distribution (SED) modelling are required for better understanding of the nature of γ-NLS1 galaxies.

The interest γ-NLS1 galaxies gained, thanks to their intriguing physical properties, led to intensive multiwavelength (MWL) monitoring of these sources. Soon after the first detection in γ-rays, PMN J0948+0022 showed a spectacular HE flare in july 2009 (Foschini et al. 2011), whose SED modelling strengthened the similarities of these sources with powerful FSRQs.

Among the variable γ-ray-detected NLS1s known to date, we have chosen two extensively studied sources, for which very well-sampled MWL data sets exist: the nearest one being 1H 0323 + 342, at a redshift of $z = 0.0625$ (Landt et al. 2017), and the highly variable PMN J0948 + 0022 at a higher redshift (z = 0.5846; Zhou et al. 2003). This selection is complemented by the source B2 0954+25A, an FSRQ with similar SED and redshift as PMN J0948+0022 (see D'Ammando et al. 2015). We have modelled the SED of different activity states (low/average and flaring) with a one-zone model including synchrotron and self-Compton emission, as well as external Compton (EC) emission on the different photon fields inside the source. Two scenarios have been tested: one where the high-energy range is dominated by up-scattering of photons from the broad-line region and another one where the up-scattering of photons from the dusty torus is the most significant.

Exploiting the available observational constraints concerning the source dimensions, energetics, and variability time-scales, we propose a common physical characterization of the variability and jet power of these sources.

Section 2 provides the description of the adopted multicomponent model and Section 3 lists the physical constraints we apply to reduce the available parameter space. Sections 4, 5, and 6 present the individual source characteristics, the data sets, and the results of our broad-band SED modelling for the three considered objects, 1H 0323+342, PMN J0948+0022, and B2 0954+25A, respectively. The results of the modelling are discussed in Section 7, where we attempt a physical characterization of the mechanisms behind the varying broad-band emission and the source energetics of the two γ-NLS1s and compare them to the FSRQ under study.

Throughout the paper, we adopt a Λ-CDM cosmology with $H_0 = 70 \, \mathrm{kms^{-1}Mpc^{-1}}$, $\Omega_m = 0.3$, and $\Omega_\Lambda = 0.7$ (Spergel et al. 2003).

2 DESCRIPTION OF THE CODE AND THE GENERAL APPROACH

While a synchrotron self-Compton (SSC) model quite accurately describes the SEDs of most BL Lac type objects, for FSRQs, which exhibit a strong Compton dominance, γ-ray emission is thought to be produced by the EC mechanism on an ambient field of soft seed photons external to the jet. This also seems to be the case for γ-NLSy1 galaxies. Seed photons relevant for one-zone models are the

direct radiation from the accretion disc and the up-scattered radiation in the X-ray corona, the reprocessed radiation from BLR clouds, or from the dusty torus (e.g. Dermer, Schlickeiser & Mastichiadis 1992; Ghisellini & Tavecchio 2009).

The multicomponent code we have developed is based on the model described by Cerruti et al. (2013) and Dermer et al. (2014). In the present version, the dust torus, disc, and corona components are described following Ghisellini & Tavecchio (2009), while the scattered components are treated following Dermer & Menon (2009) and γ-γ absorption in the BLR has been added following Dermer & Menon (2009).

The emission region is assumed to be a relativistic plasma blob of radius R_{src} that moves along the jet with bulk Lorentz factor Γ, carrying a tangled magnetic field (of intensity B) and relativistic electrons with a distribution that steepens with energies, represented here by a broken-power law (BPL) distribution in the range of [γ_{min}, γ_{max}] with a break energy γ_b and a sharp cut-off at high energy. The jet is oriented at a small angle θ with respect to the line of sight resulting in a Doppler boosting δ.

The accretion disc is described here as a multitemperature black-body spectrum peaking in the optical/UV,[1] while the hot dust in the molecular torus is a simple black body peaking in the near-infrared. The X-ray corona, above and below the inner parts of the accretion disc, is treated as a simple power-law function with an exponential cut-off at around 150 keV (Ghisellini & Tavecchio 2009). Accretion disc and corona photons will ionize the BLR, which is assumed to be a spherical shell of width ΔR expanding between an inner and an outer radius ($\Delta R \ll R_{in}, R_{out}$). We assume the BLR clouds intercept and reprocess, mainly into emission lines, a fraction of the disc luminosity (see Cerruti et al. 2013 for more details). The density of the BLR has a power-law shape within ΔR, with an index ξ fixed to $\xi = -2$ that implies that most of the ionization takes place close to the inner edge of the BLR (see Dermer & Menon (2009) and Finke & Dermer (2010) for a detailed explanation).

The torus, the corona, and the BLR luminosities are scaled to the disc luminosity through the factors τ_{IR}, τ_X, and τ_{BLR}, respectively, which are considered as free parameters. These low-energy external radiation fields are comptonized when they encounter the relativistic electrons from the blob (Dermer & Menon 2009). We consider direct interactions between the relativistic electrons and the torus, the disc and the corona, as well as interactions between BLR-scattered disc and corona photons and the blob.

The effect of both intrinsic (γ-γ opacity due to the BLR radiation field) and extragalactic background light absorption (Franceschini, Rodighiero & Vaccari 2008)) are taken into account. A list of the model parameters can be found in Table 1 and Table 2, and a detailed description of the code in Arrieta-Lobo, Boisson & Zech (2017).

In what follows, two different scenarios regarding the position of the blob (R_γ) are studied and compared to investigate the origin of the HE emission and its variability.

In the first scenario, disc&BLR-IC, the disc and BLR inverse Compton components (IC) dominate at hard X-rays and γ-ray energies, respectively ($R_\gamma < R_{BLR, in}$). The photons from the BLR are boosted in the jet frame and consequently the inverse Compton scattering of the BLR photons dominates the HE part of the SED. Since the accretion disc photons are hotter than the ones from the BLR, the disc IC component can still strongly contribute to the radiative output if the blob is close enough to the disc (Dermer &

---

[1] A geometrically thin optically thick accretion disc is considered (Shakura & Sunyaev 1973)

Table 1. Blob model parameters.

Parameter	Symbol
Bulk Doppler factor	δ
Viewing angle	θ
Radius of emitting region	R_{src}
Magnetic field intensity	B
Normalization at $\gamma = 1$	K
Low-energy spectral index	n_1
High-energy spectral index	n_2
Minimum electron Lorentz factor	γ_{min}
Break electron Lorentz factor	γ_b
Maximum electron Lorentz factor	γ_{max}
Jet height	R_γ

Table 2. External fields model parameters.

Parameter	Symbol
Disc luminosity	L_d
BH mass	M_{BH}
Accretion efficiency	$\eta = 1/12$
Corona luminosity/ Disc luminosity	τ_X
Coronal X-rays index	α_X
BLR inner radius	R_{BLR}
Dust torus temperature	T_{IR}
Dust torus radius	R_{IR}
Fraction of disc luminosity reprocessed by the BLR	τ_{BLR}
Fraction of disc luminosity reprocessed by the torus	τ_{IR}
Fraction of corona emission reflected by the BLR	$\tau_{X, BLR} = 0.01$

Schlickeiser 1993; Sikora, Begelman & Rees 1994). In this scenario, we fix τ_{IR} to 0.05. In the second scenario, torus-IC, the torus IC component dominates at γ-ray energies ($R_\gamma \sim R_{BLR, out}$). The photons from the disc and the BLR are de-boosted in the blob frame and $\tau_{BLR} = 10^{-4}$, so that the dominant contribution to external processes comes from the dusty torus.

3 PHYSICAL CONSTRAINTS

One of the main difficulties of the broadband SED modelling consists in a high number of free parameters. To reduce the number of free parameters, we can rely on observational constraints such as the variability time-scales in different frequency bands, and the measurements of the jet opening angles (when available) in order to constrain the radius of the emitting region.

The causality condition puts an upper limit to the intrinsic radius of the source: $R_{src} < c\tau\delta/(1 + z)$, where τ is the variability time-scale in a given frequency band and δ is the Doppler factor. Although variability time-scales vary from one flaring episode to another, depending also on the frequency range and the convention used to define them (flux doubling/halving time, total duration, etc.), they remain short, of the order of days or hours (especially in γ-rays). All measurements indicate compact regions in the jet to be responsible for variability in γ-rays and sometimes in X-rays and Optical/UV bands too.

As usual, we assume that $\Gamma\alpha_{int} \lesssim 1$, where Γ is the bulk Lorentz factor and α_{int} is the intrinsic opening angle of the jet. Assuming a conical jet structure, it also requires the size R_{src} of the emission region to be less than the size of the jet at the emission region location R_γ, and so $R_{src} \lesssim R_\gamma/\Gamma$.

An even modest change in θ can be reflected in large changes of δ and then of the observed flux. Intermediate values of a few

degrees were chosen for the viewing angles. We could exclude much larger or smaller values due to the (de-)boosting effect, causing the model to strongly underestimate or overestimate the overall flux. For example $\sim10°$ and $0.5°$ were estimated for 1H 0323+342 and PMN J0948+0022, respectively, by Homan et al. (2021), based on MOJAVE program data, (Lister et al. 2021), which we cannot reproduce for the modelled flux states.

The knowledge of the BH mass and of the luminosity of the accretion disc considerably help to constrain the free parameters of the model. We thus make use of the estimates available in the literature and restrict our scenarios to sub-Eddington accretion regimes. The inner radius of the BLR, $R_{BLR, in}$, is estimated from the empirical relations derived from reverberation mapping campaigns (e.g. Bentz et al. 2013; Kaspi et al. 2005) as $R_{BLR,in} \simeq 10^{17} L_{d,45}^{1/2}$ [cm] and we adopt $R_{BLR, out} = 3R_{BLR, in}$. Scattering of dust torus photons occur at larger distance $R_{IR} = 3.5 \times 10^{18} L_{d,45}^{1/2}(\frac{T_{IR}}{10^3})^{-2.6}$ [cm] (e.g. Sikora et al. 2009), where $T_{IR} \sim 1200-1500$ K to avoid sublimation of the dust grains. $L_{d, 45}$ refers to the disc luminosity in units of 10^{45} erg s^{-1}.

4 1H 0323+342

4.1 Observational constraints and physical properties

1H 0323+342 is the closest source among currently known γ-NLS1 galaxies ($z = 0.0625$, Landt et al. 2017).

1H 0323+342 is thought to be moderately radio-loud, with radio-loudness (RL) ranging from 4 to 25 (Zhou et al. 2007).

Fuhrmann et al. (2016) characterized the pc-scale jet structure and kinematics of 1H 0323+342 using multi-epoch radio VLBA[2] observations (MOJAVE[3] programme, Lister et al. (2009)), complemented with single-dish Effelsberg and IRAM[4] data. In addition to the compact stationary core, six moving knots were identified, among which five were found to have superluminal apparent velocities $\sim(1-7)$ c, suggesting relatively low viewing angle values, $\theta \leq 4°-13°$. If we make the reasonable assumption of $\theta \sim 1/\Gamma$, this constrains $\Gamma > 4.4-14.3$. Multifrequency radio light-curves, from 2010 to 2015, show a major outburst in early 2013, followed by the detection of a new radio component around 2013.5. In a more recent work, Homan et al. (2021) characterized the pc-scale jet of a wide sample of AGN from MOJAVE program for kinematics (Lister et al. 2021), including 1H 0323+342, and, assuming the median brightness temperature of their sample derive $\Gamma \sim 11$ and $\theta \sim 9.8°$ for the median state.

Foschini et al. (2009) found remarkable variations in the X-ray emission above 20 keV: the source went from a low flux, soft spectrum state in 2004 to a high flux, hard spectrum in 2006–2008, which can be interpreted as disc/corona emission dominating in 2004 and a more important jet contribution in 2006–2008. Yao et al. (2015) showed that the source presents statistically correlated variability in ultraviolet and X-ray bands, both on daily and yearly time-scales, the correlated UV/X-ray variability time-scale of days being consistent with X-ray emission from reprocessed accretion disc photons.

From long-term follow-up of the γ-ray-emitting NLSy1 galaxies by *Swift* in Optical, UV, and X-ray bands, D'Ammando (2020a) reported very short X-ray variability time-scale for 1H 0323+342 in July 2013, $\tau = 6$ ks hence $R_{src} < 1.8 \times 10^{15}$ cm assuming a

[2]Very Long Baseline Array

[3]Monitoring of Jets in AGN with VLBA Experiments

[4]Instituto de Radioastronomía Milimétrica

typical value of $\delta = 10$. A systematic analysis of all *Swift*-UVOT[5] observations in optical and UV bands of this source up to April 2019 presented in D'Ammando ([2020b]) showed a very short intrinsic variability time-scale in UV too, ~ 5.4 to 16.3 ks for 1H 0323 + 342, implying $R_{src} < (1.6-4.9) \times 10^{15}$ cm. Paliya, Stalin & Ravikumar ([2015]) reports a flux-doubling time-scale of 3.09 ± 0.85 hr during the *Fermi*-LAT flare of August 2013 ($\sim 56\,531$ MJD). This value corresponds to $R_{src} \lesssim (2-4) \times 10^{15}$ cm. All X-ray, Optical/UV, and γ-ray variability time-scales agree.

For all three sources, to assemble (quasi-)simultaneous multiwavelength data sets depicting different activity states, we took advantage of the *Fermi All-sky Variability Analysis* web tool[6] (FAVA), a tool that blindly searches for transients over the entire sky observed by the LAT (Abdollahi et al. [2017]) and retrieved data from the *Fermi*-LAT Light Curve Repository[7] (Fermi Large Area Telescope Collaboration ([2021])). The flaring and quiescent states identified in HE were then cross-matched with *Swift* X-rays observations.

For most of the time, the γ-ray flux did not much exceed the value averaged over time (see Fig. A1). The only prominent flare occurred in August 2013, featuring a much harder spectrum (Sahakyan, Baghmanyan & Zargaryan [2018]). During this flare, the flux-doubling time was as short as 0.49 ± 0.17 day (Baghmanyan & Sahakyan [2018]), implying the emission is produced in a compact region, $R_{src} \lesssim 1.2 \times 10^{15}$ cm assuming $\delta = 10$.

The BH mass of 1H 0323+342 was estimated to be $(1.5-2.2) \times 10^7 M_{\odot}$ by Landt et al. ([2017]) using Hα, Hβ, and Paα line width and continuum luminosities. It is consistent with the value of $(1.8-3) \times 10^7 M_{\odot}$ obtained by Zhou et al. ([2007]). Short X-ray variability time-scales from a deep *Suzaku* observation also suggest a relatively small mass of the BH, of $M_{BH} \sim 10^7 M_{\odot}$ (Yao et al. [2015]).

Kynoch et al. ([2018]) observationally constrained the external photon fields of 1H 0323+342 through a quasi-simultaneous near-IR, optical and X-ray data set, allowing to narrow the L/L_{Edd} range to 0.6–0.8 for a non-rotating Schwarzschild BH. Very high spin values and super-Eddington case were rejected because of the poor quality of the fit to the data in that case. The luminosity of the accretion disc was estimated to be 2.1×10^{45} erg s^{-1}.

For our study, we consider three activity states (low, intermediate, and high) and investigate the evolution of the jet power of 1H 0323+342 (see Table 3).

4.2 The data set

The low activity state SED has been reported in Kynoch et al. ([2018]). The *Fermi*-LAT low state from August to September 2015 is indeed a non-flaring period (see Fig. A1). Contrary to the general case where low states observed by *Fermi*-LAT are rather intermediate states since γ-NLS1 galaxies tend to be undetected during very low flux phases, 1H 0323+342 went through a genuinely low activity phase during 2015 August–September. Quasi-simultaneous GNIRS IR spectral data retrieved from Kynoch et al. ([2018]) are added for completeness in the SEDs. The HE data are complemented with the optical and X-ray data closest in time with this very low *Fermi* state: simultaneous *XMM-Newton* (Optical Monitor and EPIC) data. *Swift*-XRT observations reported by D'Ammando ([2020a]) show one of the lowest X-ray fluxes of 1H 0323+342 ever measured with *Swift*

Table 3. Quasi-simultaneous observations of 1H 0323+342.

Instrument	Time period	MJD
Low state		
Fermi-LAT	2015 August 1–September 30	57235–57295
XMM-Newton	2015 August 23	57 257
GNIRS	2015 September 16	57 281
Intermediate state		
Fermi-LAT	2008 November 5–December 5	54775–54805
Swift	2008 November 16	54 786
High state		
Fermi-LAT	2013 August 27–31	56531–56535
Swift	2013 August 30	56 534

during this epoch. Only at the very end of the selected *Fermi*-period, the X-ray flux reaches a high value. The corresponding data points are depicted in green in Fig. 1 and C1.

We model the flaring state from August 2013 that corresponds to the largest high energy flux measured up to date for 1H 0323+342 (see Fig. A1 and 'F3' flaring state presented in Paliya et al. ([2014])). The MWL data used to build the flaring state SED are retrieved from Paliya et al. ([2014]) (Table 3) and depicted in orange (see Fig. 1 and C1). D'Ammando ([2020a]) reports the analysis of all *Swift* observations available up to April 2019 and show 1H 0323+342 to be at maximum in X-rays and optical during this major γ-ray flare, with a significantly hardened spectrum.

The quiescent state of 2008, modelled by Paliya et al. ([2014]), turns out to rather be an intermediate HE state (Fig. A1), but it corresponds to very low *Swift*-XRT and UVOT flux levels, among the lowest ever measured for 1H 0323+342. The corresponding data points are depicted in yellow in Fig. 1 and C1.

For completeness, we also included in the SEDs NuSTAR observations carried out during 2014 March 15–18 (MJD 56731–56733) (Landt et al. [2017]) along with the contemporaneous Effelsberg radio data taken during 2014 March 01–11 (MJD 56717–56727) (included in the F-Gamma program (Angelakis et al. [2015])), plotted in blue. Although not simultaneous with the selected low and high states, NuSTAR data are particularly interesting for the modelling purposes since they cover the hard X-ray part of the spectrum as do the catalogue data from the *Swift*-BAT 105-month all-sky survey[8](Oh et al. [2018]).

Archival data points are extracted from SSDC database[9] and depicted in grey.

4.3 SED modelling

In the following, we use $L_d = 2 \times 10^{45}$ erg s^{-1}, $M_{BH} = 2 \times 10^7 M_{\odot}$, and $\theta = 5°$, corresponding to the lower limit determined by Fuhrmann et al. ([2016]). We could exclude larger values due to deboosting effect, causing the model to strongly underestimate the overall flux. The Eddington ratio l_{Edd}[10] is then 0.80. The distance of the BLR from the central BH, $R_{BLR, in}$, constrained by the disc luminosity, is set to 4.77×10^4 R$_G$.

---

[5]Ultra-Violet Optical Telescope
[6]https://fermi.gsfc.nasa.gov/ssc/data/access/lat/FAVA/
[7]https://fermi.gsfc.nasa.gov/ssc/data/access/lat/LightCurveRepository/about.html

[8]https://swift.gsfc.nasa.gov/results/bs105mon/
[9]https://www.ssdc.asi.it
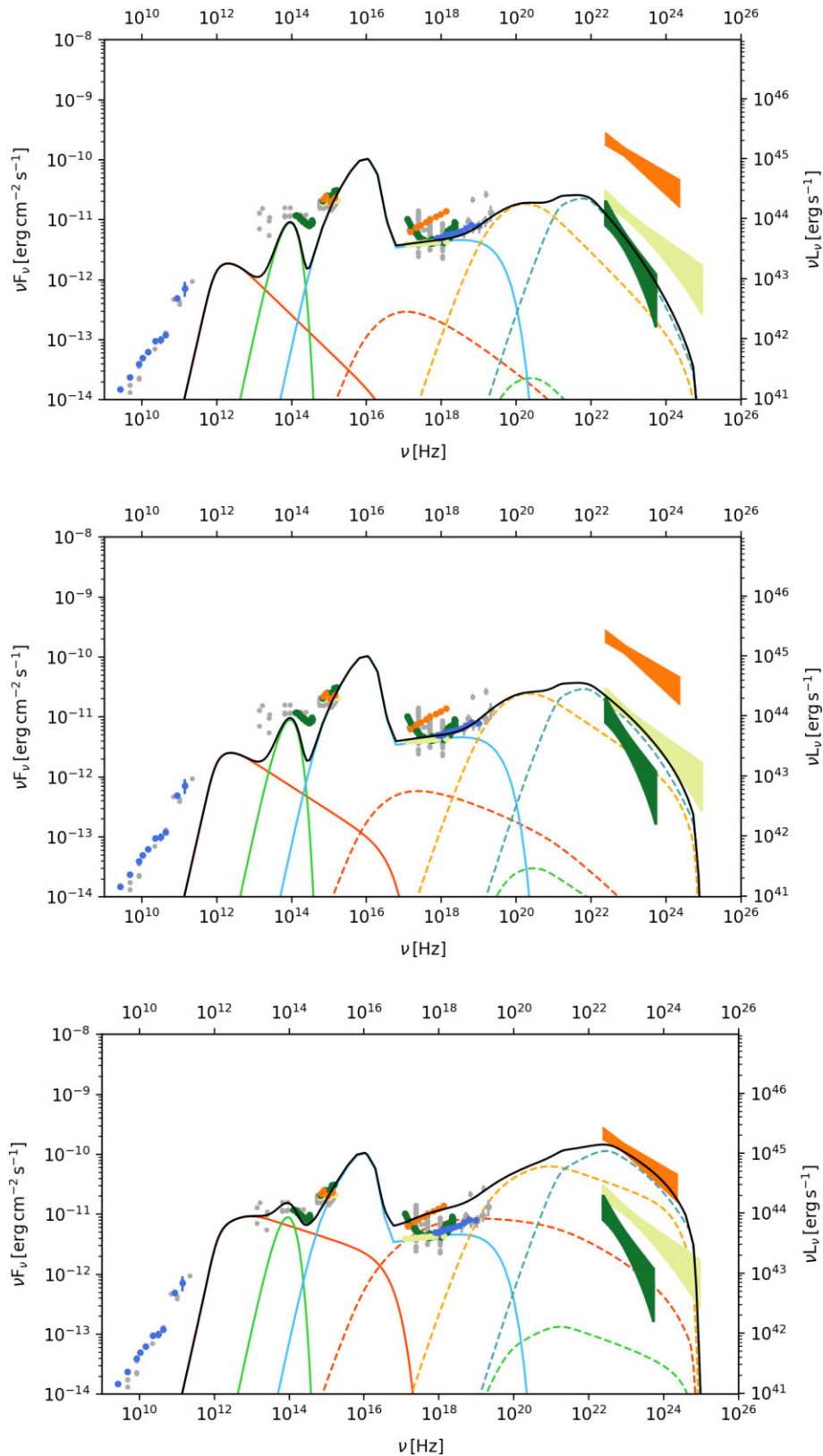[10]Defined as the ratio of the disc luminosity L_d over the Eddington luminosity $L_{Edd} = 1.3 \times 10^{38} \frac{M_{BH}}{M_{\odot}}$ erg s^{-1}

Figure 1. Disc&BLR-dominated scenario for 1H 0323+342. Direct emission components are presented in solid lines and the associated reprocessed components are depicted in dashed lines of the same colour (red for synchrotron and SSC emission, light green for direct torus emission and EIC-torus component, light blue for the direct emission of the accretion disc and corona, whereas the dashed light blue lines represent the IC scattering of the BLR photons by energetic electrons of the blob. Orange dashed lines refer to the emission produced by the IC scattering of the accretion disc photons. The data points presented here (archival and quasi-simultaneous) are dereddened and deabsorbed. See text for more details.

Table 4. Model parameters for the different scenarios considered for 1H 0323+342. Input parameters: (a) redshift, (b) viewing angle, (c) BH mass, (d) gravitational radius size, (e) disc luminosity, (f) Eddington ratio, (g) mass accretion rate, (h) Doppler factor of the blob, (i) particle density normalization (at $\gamma = 1$), (j) size of the emitting region, (k) magnetic field, (l) and (m) first and second indices of the broken power-law particle distribution, (n), (o), and (p) minimum, break, and maximum electron energies, respectively, (q) dusty torus temperature, (r) reprocessing factor of the torus, (s) and (t) slope and reprocessing factor of the corona, (u) blob–BH distance, (v) and (w) reprocessing factor and inner radius of the BLR. Derived parameters: (1) ratio of electron distribution kinetic energy density and magnetic field energy density, (2) particle density, (3) electron energy density, and (d) total jet power.

Source description						
z [a]			0.0625			
θ (°) [b]			5			
M_{BH} [M$_\odot$] [c]			2×10^7			
R_G [cm] [d]			2.95×10^{12}			
L_{Disc} [erg s^{-1}] [e]			2×10^{45}			
l_{Edd} [f]			0.79			
$\dot{m}$ [M$_\odot$/yr] [g]			0.42			
Scenario	Disc & BLR			Torus		
State	Low	Intermediate	Flare	Low	Intermediate	Flare
δ [h]	9	9	10	9	9	11
K [1/cm^3] [i]	4×10^6	5×10^6	8.4×10^6	7.4×10^6	5.0×10^6	1.3×10^7
R_{src} [cm] [j]	1.15×10^{15}	1.15×10^{15}	1.01×10^{15}	1.40×10^{16}	1.43×10^{16}	1.34×10^{16}
B [G] [k]	2.3	2.3	2.3	0.30	0.30	0.30
n_1 [l]	2.2	2.2	2.2	2.7	2.7	2.7
n_2 [m]	4.2	3.8	3.4	4.7	4.0	3.9
γ_{min} [n]	50	50	50	500	500	500
γ_b [o]	150	150	280	600	650	680
γ_{max} [p]	2×10^4	2×10^4	2×10^4	4×10^4	4×10^4	4×10^4
T_{IR} [K] [q]	1200	1200	1200	1200	1200	1200
τ_{IR} [r]	0.05	0.05	0.05	0.25	0.25	0.25
α_X [s]	0.9	0.9	0.9	0.9	0.9	0.9
τ_X [t]	0.15	0.15	0.15	0.17	0.17	0.17
R_γ [R$_G$] [u]	2.5×10^3	2.5×10^3	2.5×10^3	1.5×10^5	1.5×10^5	1.5×10^5
τ_{BLR} [v]	0.28	0.28	0.28	1×10^{-4}	1×10^{-4}	1×10^{-4}
R_{in}^{BLR} [R$_G$] [w]	4.77×10^4	4.77×10^4	4.77×10^4	4.77×10^4	4.77×10^4	4.77×10^4
u_e/u_b [1]	9.72	12.87	29.54	10.95	9.75	27.14
n_e [1/cm^3] [2]	2.57×10^4	3.27×10^4	6.07×10^4	68.56	55.44	1.51×10^2
u_e [erg cm^{-3}] [3]	2.05	2.71	6.22	3.92×10^{-2}	3.49×10^{-2}	9.72×10^{-2}
$P_{jet,tot}$ [erg s^{-1}] [4]	3.82×10^{44}	5.02×10^{44}	1.40×10^{45}	2.39×10^{44}	2.28×10^{44}	1.63×10^{45}

For three activity states, two scenarios, disc and BLR-dominated (disc&BLR) and torus-dominated, are tested and reported in Fig. 1 and C1, respectively. The model changes from lower to higher activity state allowing only the compact jet parameters to vary, while all parameters linked to the external photon fields remain constant. Input parameters as well as physical quantities derived from the model are shown in Table 4.

The electron distribution is strongly constrained by the *Fermi*-LAT spectral shape. The clear hardening of the GeV spectrum during the flaring state, compared to the quiescent ones, imposes a hardening of the electron distribution. The transition from a quiescent to a more energetic state is simply described by a denser and more energetic blob within the jet (larger electron density and Doppler factor).

In the disc&BLR scenario, reasonable account of the SEDs is achieved with an emitting region located at $R_\gamma = 2.5 \times 10^3$ [R$_G$]. The relativistic jet peaks at submillimetre frequencies. Kynoch et al. (2018) attributed the IR part of the SED, as defined by the Spitzer and the WISE data, to thermal emission from the extended dusty torus, thus requiring that the synchrotron emission does not contribute substantially to it. In the highest activity state, this may not be fulfilled, but those IR data are not simultaneous nor contemporaneous

and for an even more powerful jet, one might have a dominating synchrotron component. The thermal disc emission is a major contribution at optical/UV wavelengths. Hard X-ray data are ascribed to a combination of the direct corona emission and jet radiation, the contribution from SSC radiation dominating in the flaring state.

In the second scenario, the blob is located at the outermost edge of the BLR. A much larger torus reprocessing factor is needed here, $\tau_{IR} = 0.25$, to account for the high energy emission. The large fraction of disc reprocessed by the dusty torus makes its direct emission to peak higher than the archival data regardless of the activity state. The peak of the electron distribution occurs at much higher energies in the torus-dominated case, so all IC components of the model are shifted to higher energies. The electron energy densities are much lower in the torus-dominated scenario, which implies less synchrotron self-absorption at radio frequencies. In this scenario, the size of the emission region is in contradiction with the variability constraint we have adopted.

In both scenarios, our model underestimates the UV and X-ray radiation during the quiescent state. This could be ascribed to our simple description of the accretion flow at these frequencies as a multitemperature blackbody.

5 PMN J0948+0022

5.1 Observational constraints and physical properties

PMN J0948+0022, with a moderately high redshift ($z = 0.5846$, Zhou et al. (2003)), is classified as a typical radio loud NLSy1 galaxy with strong ($RL \gtrsim 10^3$) and variable radio emission. Its inverted radio spectrum and very high brightness temperature ($\simeq 10^{13}$ K) derived from variation of the radio flux suggested the presence of a relativistic jet strongly beamed towards the observer (Zhou et al. (2003)). This was later confirmed when PMN J0948+0022 turned out to be the first NLS1 galaxy detected in γ-rays by the *Fermi*-Large Area Telescope (Abdo et al. (2009a)).

VLBI monitoring during the first γ-ray flare ever detected in an NLS1, which occurred in July 2010, with shortest and even intraday variability time-scales (Foschini et al. (2011)) revealed polarization, change of the EVPA vector of about 90° and a variable radio spectral shape, probably related to the γ-ray flare. The source is seen as a bright compact core, with large brightness temperatures (Giroletti et al. 2011), indicating a heavy Doppler beaming. Since then its variable radio spectrum has been intensively monitored (see e.g Angelakis et al. (2015) and Lähteenmäki et al. () for a review). The existence of several superluminal components in the jet of this source points towards a small viewing angle and large Lorentz factor (e.g. Homan et al. 2021).

Although PMN J0948+0022 already showed a moderately enhanced γ-ray emission during 2009 March–July (Abdo et al. 2009b), the outburst from July 2010 was a factor of ∼2 greater, exceeding a peak flux value of ∼ 10^{-6} ph cm^{-2} s^{-1} (corresponding to an observed luminosity of ∼ 10^{48} erg s^{-1}) in the 0.1–100 GeV energy range, for the first time in this type of source. Long-term MWL monitoring from Foschini et al. (2012) showed that the flare from July 2010 is accompanied by a more progressive flaring episode detected in radio wavebands (at 15 GHz and 86 GHz). The source showed prolonged activity in radio in 2011 as well as in γ-rays.

From a systematic analysis of about 10 years of *Swift* observations of NLSy1 galaxies, D'Ammando (2020b) reported rapid variability in optical bands for PMN J0948+0022, ranging from very short (minimum) intrinsic variability time-scale of ∼3.3 ks to ∼30 ks, which translates into $R_{src} < (1.1–8.8) \times 10^{15}$ cm, assuming a Doppler factor of 10. Similarly, γ-ray variability time-scale values of 74.6 ± 27.6 hrs (Paliya et al. 2015), 2.3 ± 0.5 days (Foschini et al. 2012), and 3–30 days reported by Calderone et al. (2011) correspond to $R_{src} < (3–7) \times 10^{16}$ cm, $R_{src} < (3–5) \times 10^{16}$ cm, and $(0.5–6) \times 10^{17}$ cm, respectively, assuming a Doppler factor of 10. Sahakyan et al. (2018) even quote 18.9 hrs for the extremely active state during the period December 2012–January 2013. The large dispersion in the estimations is due to different variability trends in different spectral domains and binning during extreme flaring activity episodes compared to intermediate/quiescent ones. Indeed PMN J0948+0022 is a very active γ-ray emitter; the source is alternatively in its flaring or quiescent states (see Fig. A2). We keep the most restrictive upper limit $R_{src} \lesssim (1.1–8.8) \times 10^{15}$ cm.

A lower limit on the BH mass of $10^8 M_\odot$ was obtained from accretion disc fitting of *Swift*-UVOT data (Abdo et al. 2009a; Calderone et al. 2013), in agreement with the BH mass range obtained by Zhou et al. (2003): $M_{BH} \sim (4.0 \times 10^7 – 8.1 \times 10^8) M_\odot$ deduced with the assumption that the line emitting cloud motions are virialized. The estimate from Yuan et al. (2008) $\sim 10^7 M_\odot$ remains significantly smaller and inconsistent with the previous values. More generally, Chiaberge & Marconi (2011) found that taking into account radiation pressure correction on the BLR clouds in the virial techniques results

in higher BH masses, which illustrates the complexity of BH mass measurements. High radio-loudness parameter seems to favour larger BH masses too. Since different independent techniques seem to converge towards $M_{BH} \gtrsim 10^8 M_\odot$, we keep $M_{BH} = 1.5 \times 10^8 M_\odot$ as assumed for modelling in Abdo et al. (2009a).

Disc luminosity has been estimated to $L_d = 9 \times 10^{45}$ erg s^{-1} obtained from SED fitting of the 2009 state (see Abdo et al. (2009b, 2009c) for more details), and $L_d = 5.7 \times 10^{45}$ erg s^{-1} from modelling of the 2011 and 2013 states in D'Ammando et al. (2015). We used $L_d = 9 \times 10^{45}$ erg s^{-1} because lower values did not provide enough disc luminosity for EIC scattering of the BLR and torus photons to account for the observed elevated HE flux levels.

5.2 The data set

Fermi-LAT detected the most powerful flaring activity from PMN J0948+0022 between 2012 December and 2013 January, triggering *Swift*, VERITAS[11] and other MWL observations (D'Ammando et al. 2015). VERITAS observations resulted in upper limits. A strong optical/UV and X-ray flare occurred quasi-simultaneously with the γ-ray flare, implying that the jet emission is the dominant mechanism. One of the most prominent radio flares from this source at 15 Ghz (Lähteenmäki et al. 2017) is recorded a few days later. Bulk Lorentz factors as high as 30 were used by D'Ammando et al. (2015) to model the flare SED, which is not surprising given the large observed luminosities and BL Lac-type shape, with a completely jet-dominated SED at that time. Being interested in the disc-dominated cases, we discard the 2013 flaring event from our analysis.

In a compromise between photon statistics (see Fig. A2) and reasonable MWL coverage, we consider, for the low state, the data set from D'Ammando et al. (2015) that features *Fermi*-LAT data from May 22 to June 11, *XMM-Newton* on 2011 May 28–29 and Effelsberg radio data at 15 and 32 GHz on 2011 May 24, avoiding nearby HE outburst phases (especially on 2011 June 21, see e.g. Foschini et al. 2012). This state is particularly interesting since the soft-excess is clearly visible in the X-ray data, and a hard power-law spectrum describes the X-ray data beyond 2.5 keV (Bhattacharyya et al. 2014; D'Ammando et al. 2014). This contemporaneous data set (see Table 5) is depicted in green in Figs 2 and C2.

The most prominent γ-ray outburst from 2010 July occurred during the course of a dedicated MWL campaign performed during 2010 July–September (Foschini et al. 2011). Only one X-ray observation close to the outburst could be performed by *Swift* on July 3rd, about 4 days before the γ-ray outburst. It can be seen from Fig. A3 that the corresponding *Swift*-XRT and UVOT fluxes are indeed only moderately high.

The data set for the 2010 flare is taken from the study by Foschini et al. (2012) as they feature mostly simultaneous or contemporary data. From the five different epochs presented in their paper, we have considered that of 2010 July 8 (MJD 55386), which corresponds to the first documented γ-ray outburst of the source, as a high state for modelling. For their data set, Foschini et al. (2012) considered *Fermi*-LAT data integrated over one day, while *Swift* observations from July 3 are considered. Effelsberg radio data from 2010 September 18 (MJD 55457) retrieved from Angelakis et al. (2015) are also included. The contemporaneous SED is depicted in orange on Figs 2 and C2. Mid infrared photometry for the source was obtained by

---

[11] Very Energetic Radiation Imaging Telescope Array System; https://veritas.sao.arizona.edu/
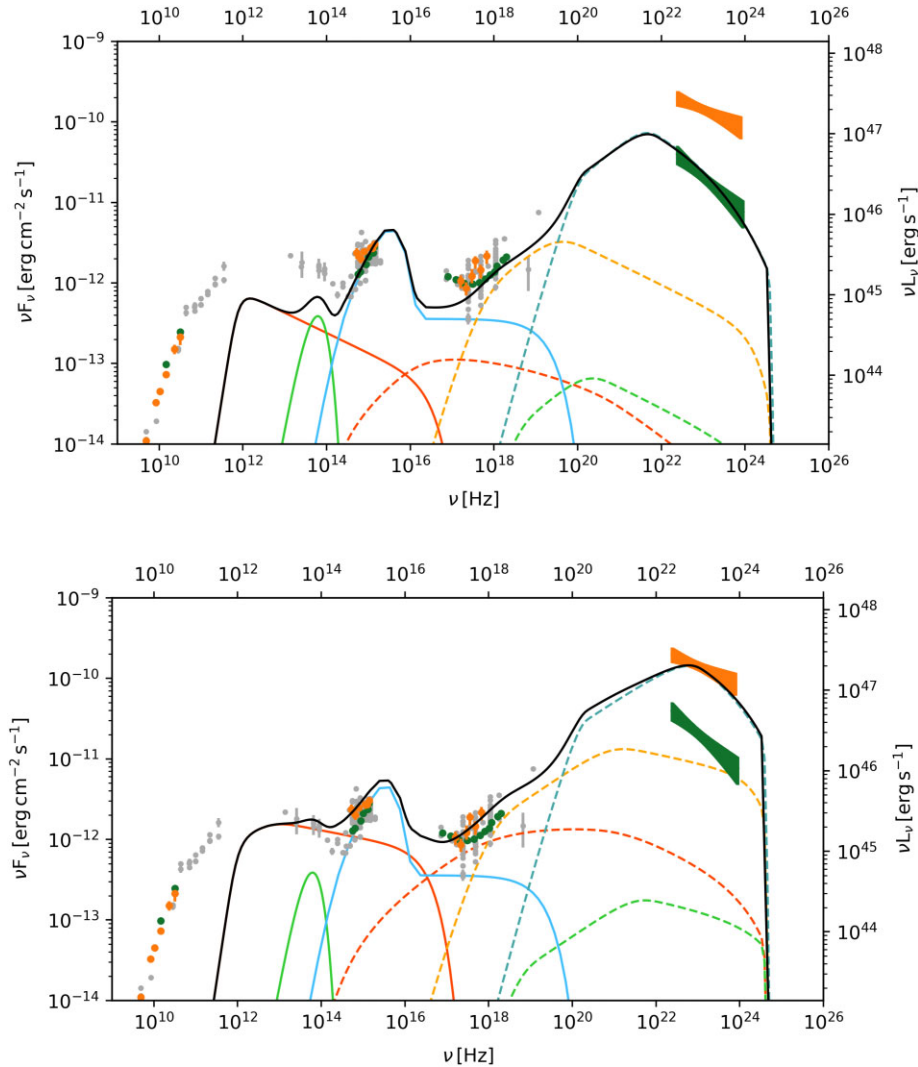
Figure 2. Disc&BLR-dominated scenario for PMN J0948+0022. The description of the model components and the data is the same as in Fig. 1.

the Wide-field Infrared Survey Explorer[12] (WISE) during May 14–15 (MJD 55330–55331) and November 20–21 (MJD 55520–55521), that is right before and after the period considered here. The average flux per period in grey along with archival data points was extracted from the ASDC[13] database.

To build the SED, we analysed *Fermi*-LAT data recovered from the *Fermi* Science Support data server;[14] details on the analysis can be found in Appendix B. Assuming a power-law spectral shape, a binned likelihood analysis of the flaring state from July 7 to July 9 (MJD 55384–55386) yields a detection with a test statistic TS = 175.7 (i.e. 13.3σ) in the 0.1–100 GeV energy range, $F_{0.1-100GeV}$ = $(1.07 \pm 0.15) \times 10^{-6}$ ph cm^{-2} s^{-1} for $\Gamma = 2.22 \pm 0.12$. For the period between 2011 May 22 and June 11 (MJD 55703–55723), the analysis yielded a detection with TS = 107.2 (i.e. 10.4σ) in the 0.1–100 GeV energy range, an integral flux $F_{0.1-100GeV}$ = $(2.12 \pm 0.35) \times 10^{-7}$ ph cm^{-2} s^{-1} for a softer spectral slope, $\Gamma = 2.50 \pm 0.14$,

than the high state. The highest energy photon from the source is below 4 GeV.

5.3 SED modelling

All models assume a viewing angle of $\theta = 3°$ (Foschini et al. 2011), a black-hole mass of $M_{BH} = 1.5 \times 10^8 \, M_\odot$, and a disc luminosity of $L_d = 9 \times 10^{45}$ erg s^{-1} corresponding to an Eddington ratio l_{Edd} = 0.48. The distance of the BLR from the central BH, $R_{BLR, in}$, constrained by the disc luminosity, is set to $1.5 \times 10^4 \, R_G$.

Again, the intermediate and the flaring states of PMN J0948+0022 were modelled in a disc&BLR-IC scenario where the blob is below the BLR and in a torus-IC scenario where the emission region is at the outermost edge of the BLR. The results of the broad-band modelling of the two activity states for PMN J0948+0022 are shown in Fig. 2 and C2 in the BLR- and torus-dominated scenarios, respectively, and the corresponding parameters are given in Table 6.

In the disc&BLR-dominated scenario, the BLR reprocesses 40 per cent of the disc luminosity and the HE emission is explained by the IC scattering of the BLR photons by relativistic electrons of the blob. The X-ray corona has a fixed luminosity $L_X = 0.3 \, L_d$. The X-ray spectrum is mainly produced by the disc-IC component for both low

Table 5. Observations of PMN J0948+002.

Instrument	Time period	MJD
Low/intermediate state		
Fermi-LAT	2011 May 22–June 11	55703–55723
XMM-Newton	2011 May 28–29	55709–55710
Effelsberg	2011 May 24	55 705
High state		
Fermi-LAT	2010 July 7–9	55383.5–55389.5
Swift (UVOT & XRT)	2010 July 3	55 380
Effelsberg	2010 September 18	55 457

and high states. However, in the high state, a strong contribution from the non-thermal SSC emission from the jet is required in addition to the disc-IC emission.

The flaring state of the source is again explained by larger Doppler factors in both scenarios. In the disc&BLR-IC scenario, the flare also features a denser blob, but this is not the case in the torus-IC solution. A 'harder when brighter' trend is also observed at γ-rays. In both scenarios, the flaring states feature larger electron break energies.

In the torus-IC scenarios, similar to 1H 0323+342, the synchrotron self-absorption is much reduced with respect to the disc&BLR-dominated scenario, due to lower electron densities. IR frequencies are described by the torus emission in both scenarios (let us recall there are not simultaneous data at these frequencies though), and the optical UV excess is well described by the multitemperature accretion disc in both scenarios too.

A rather large reprocessing factor of the dusty torus $\tau_{IR} \sim 35$ per cent (see Table 6) is necessary to explain the HE emission in the torus-dominated scenario. A large corona luminosity, about half of the disc luminosity, is also required in this scenario to account for the observed X-ray emission.

In the disc&BLR scenario, hard X-ray emission is explained mostly by the disc IC component with minor contributions from the corona and SSC components. In the torus-IC scenario, a combination of the X-ray corona and SSC from the jet account for the hard X-ray radiation. As for 1H 0323+342, in the torus scenario, the size of the emission region is in contradiction with the variability constraint we have adopted.

Because the soft X-ray excess is usually ascribed to another component whose origin is still debated (e.g. D'Ammando et al. 2014; Bhattacharyya et al. 2014), we accept deviation of our models in this frequency band.

6 B2 0954+25A

6.1 Observational constraints and physical properties

B2 0954+25A is the most distant source of our small sample (z = 0.712; Burbidge & Strittmatter 1972). This source is missing from general studies of the γ-ray-emitting NLS1 class galaxies (e.g. Paliya et al. 2019; Foschini 2020), certainly due to its habit of completely changing its emission spectrum. Indeed B2 0954+25A has been observed in the optical in (at least) three different emission states: partially jet-dominated in 1987 (Jackson & Browne 1991), disc dominated in 2004 (Abazajian et al. 2009), and totally jet dominated in 2006 (Adelman-McCarthy et al. 2006).

Through a detailed reanalysis of the intensity and shape of the Balmer line in those spectra, Calderone et al. (2012) did find a likely value of FWHM(Hβ) $\sim$2800 kms^{-1}, just slightly above the

commonly adopted classification criterion for NLS1 sources. They consequently revisited the estimation of the black-hole mass by means of virial method and mass–stellar dispersion relation ($M - \sigma*$), and derived a small black-hole mass, $M_{BH} = (1–3) \times 10^8 M_\odot$. Calderone et al. (2012) propose this source to be a transition object between FSRQs and γ-loud NLS1s due to its characteristics of both classes, and the strong similarity of its SED (in the disc-dominated state) to that of PMN J0948+0022. Calderone et al. (2012) also provides an estimate of the disc luminosity $L_{bol,Disc} = 10^{46}$ erg s^{-1}, inferred from the measurement of Hβ line luminosity with a BLR covering factor of 0.1 ($L_{bol,Disc} = 10 L_{BLR}$) and obtained a compatible value of 1.13×10^{46} erg s^{-1} from SED modelling. The higher value of $L_{bol,Disc} = 10^{47}$ erg s^{-1} obtained from the SDSS catalogue (Shen et al. 2011) is rejected due to the spectrum being taken in a jet-dominated state.

B2 0954+25A is a compact radio-loud AGN with a flat radio spectrum. While usually flat, the radio spectrum of the source becomes inverted during burst activity (Torniainen et al. 2005). Apparent superluminal motions (12c, Kellermann et al. 2004) suggest a small viewing angle θ (3°–6°; Calderone et al. 2012).

B2 0954+25A is not as intensively studied as 1H 0323+342 and PMN J0948+0022, but radio variability is also seen for this source in the MOJAVE data set at 15 GHz.[15]

The source is known for high variability amplitudes both in optical/UV and X-ray bands (about a factor of 10 difference on timescales of $\sim$year) as shown by the data sets presented in Calderone et al. (2012). In the X-ray energy range, B2 0954+25A has been observed by several facilities, such as Einstein, *Chandra*, *ROSAT* or *Swift*-XRT, but observations are scarce and depict essentially low states, except for the Einstein 1979 observation.

Contrary to genuine γ-NLS1s that have been intensively observed, with variability features studied in depth since their discovery in γ-rays, B2 0954+25A is poorly monitored and poorly documented, the only detailed MWL study being from Calderone et al. (2012).

A monthly binned *Fermi*-LAT light curve is displayed in Fig. A3 showing low statistic data and a broad variability pattern. Only very few *Swift* observations were taken since the launch of the *Fermi* satellite. We analysed all available *Swift*-XRT X-ray observations for B2 0954+25A together with the few simultaneous *Swift*-UVOT follow-ups (see Table B1 and Table B2).[16] The fractional variability is low, $F_{var} = 0.28 \pm 0.02$. However, one should keep in mind that it is the most distant source of our sample and that data only cover nine epochs, such that the observed variability might not be statistically meaningful.

6.2 The data set

Chandra observations carried out on 2009 January 20 and presented in Calderone et al. (2012) showed a low X-ray state and are used to constrain the X-ray domain of the SED, as it coincides with a low *Fermi* state (Fig. A3). Because of the lack of significant variability in the γ-rays of B2 0954+25A over the years (see e.g. available FAVA[17] or Fig. A3 light curves), we consider that the long-term 4-year averaged (3FGL) *Fermi* spectrum (Acero et al. 2015), where the source is detected with a significance of approximately 15.9σ, an integrated flux value in the 0.1–100 GeV energy range of $F_{1-100GeV} = (8.88 \pm 0.94) \times 10^{-10}$ ph cm^{-2} s^{-1}, and a PL index

---

[15]https://www.cv.nrao.edu/MOJAVE/

[16]see next section and Appendix for details. Data are reported in Fig. A3

[17]https://fermi.gsfc.nasa.gov/ssc/data/access/lat/FAVA/

Table 6. Model parameters for the different scenarios considered for PMN J0948+0022. The description of the model input and model-derived parameters is the same as in Table 4.

Source description				
z		0.5846		
θ (°)		3		
M_{BH}		1.5×10^8		
R_G [cm]		2.22×10^{13}		
L_{Disc} [erg s^{-1}]		9×10^{45}		
l_{Edd}		0.48		
$\dot{m}$ [M$_\odot$ yr^{-1}]		1.90		
Scenario	Disc & BLR		Torus	
State	Average	Flare	Average	Flare
δ	16	19	10	12
K [1 cm^{-3}]	1×10^6	4×10^6	8.2×10^5	1×10^6
R_{src} [cm]	3.8×10^{15}	2.25×10^{15}	9.37×10^{16}	9.35×10^{16}
B [G]	1.5	1.5	0.20	0.12
n_1	2.1	2.3	2.7	2.7
n_2	3.5	3.2	3.9	3.5
γ_{min}	10	10	450	450
γ_b	80	300	900	1×10^3
γ_{max}	2×10^4	2×10^4	3×10^4	3×10^4
T_{IR} [K]	1200	1200	1200	1200
τ_{IR}	0.05	0.05	0.35	0.35
α_X	1.0	1.0	1.0	1.0
τ_X	0.3	0.3	0.5	0.5
R_γ [R$_G$]	1.8×10^3	1.8×10^3	4.5×10^4	4.5×10^4
τ_{BLR}	0.40	0.40	1×10^{-4}	1×10^{-4}
R_{in}^{BLR} [R$_G$]	1.5×10^4	1.5×10^4	1.5×10^4	1.5×10^4
u_e/u_b	17.75	44.96	5.16	19.80
n_e [1 cm^{-3}]	6.91×10^4	1.56×10^5	13.13	16.82
u_e [erg cm^{-3}]	1.59	4.03	8.21×10^{-3}	1.13×10^{-2}
$L_{jet,tot}$ [erg s^{-1}]	4.17×10^{46}	1.13×10^{47}	8.12×10^{45}	3.15×10^{46}

$\Gamma = 2.44 \pm 0.07$, is a good proxy for a low-state γ spectrum. Corresponding data points are depicted in green (Fig. 3, Fig. C3).

Fermi did not start its operation until 2008, so no contemporary GeV data are available for the high X-ray state of 2007. Since then the source went through only two broad flaring episodes at high energy as can be seen from Fig. A3, from 2010 January–July (MJD 55200–55400) and in 2016 November ($\sim$ MJD 57700). Both flaring states have contemporaneous *Swift* data. The flaring episode in 2016 showing a jet-dominated SED (see below), we chose to model the 2010 flare. WISE observed B2 0954+25A in 2010 May 7–8 and November 14–15, the former being contemporaneous with the flaring episode of 2010 January–July (Table 7). The average flux value of the corresponding period is plotted in orange, the second observation epoch (for which only two bands are available out of four) depicted in grey along with archival data points extracted from the ASDC database.

We analysed the *Fermi*-LAT data from the flaring epoch from 2010 January (MJD 55200) to 2010 July (MJD 55400); assuming a power-law spectral shape, a binned likelihood analysis yields a detection with a test statistic TS = 212 (i.e. 14.6σ), an integrated flux in the 100 MeV–100 GeV energy range of $(5.19 \pm 0.65) \times 10^{-7}$ ph cm^{-2} s^{-1} and a photon index $\Gamma = 2.42 \pm 0.09$.

We also analysed the *Fermi*-LAT data from the 2016 November flaring episode. When combined with the *Swift*-XRT/UVOT data, it clearly shows a jet-dominated SED, so this state is discarded from our study.

All available *Swift* observation epochs of B2 0954+25A were analysed and the results can be found in Table B1 and Table B2, for XRT and UVOT instruments, respectively. The X-ray data used to build the SED correspond to the longest exposure ($\sim$ 7ks) observation of the source by *Swift*-XRT, on the 1st of 2007 June . Due to poor statistics, no good spectral information could be derived from most of the nine epochs. The detection of this source in the X-ray band seems to require an active state. In addition to the epoch with the best statistics, we use the data points from the observation closest in time with the flaring episode, from 2010 June 15 , which are depicted in red in Fig. 3 and C3. Note that they both are compatible. *Swift*-UVOT simultaneous observation were taken in only one filter: UVM2($\lambda = 224.6$ nm). UVM2 band fluxes during both flaring states are almost two times larger than the two other low-optical UV states found immediately after the decay phases. The corresponding SED is depicted in orange (Fig. 3, Fig. C3).

The archival data used to build the SED are extracted from the ASDC database and from Calderone et al. (2012). For completeness, all UVOT fluxes that are not simultaneous with the considered epochs are added in grey.

6.3 SED modelling

All models of the broad-band SED of B2 0954+25A assume a BH mass of $1.5 \times 10^8 M_\odot$, a disc luminosity of $L_d = 1.13 \times 10^{46}$ erg s^{-1}, and a viewing angle of $\theta = 3°$ (similar to 3.3° given by Homan et al.
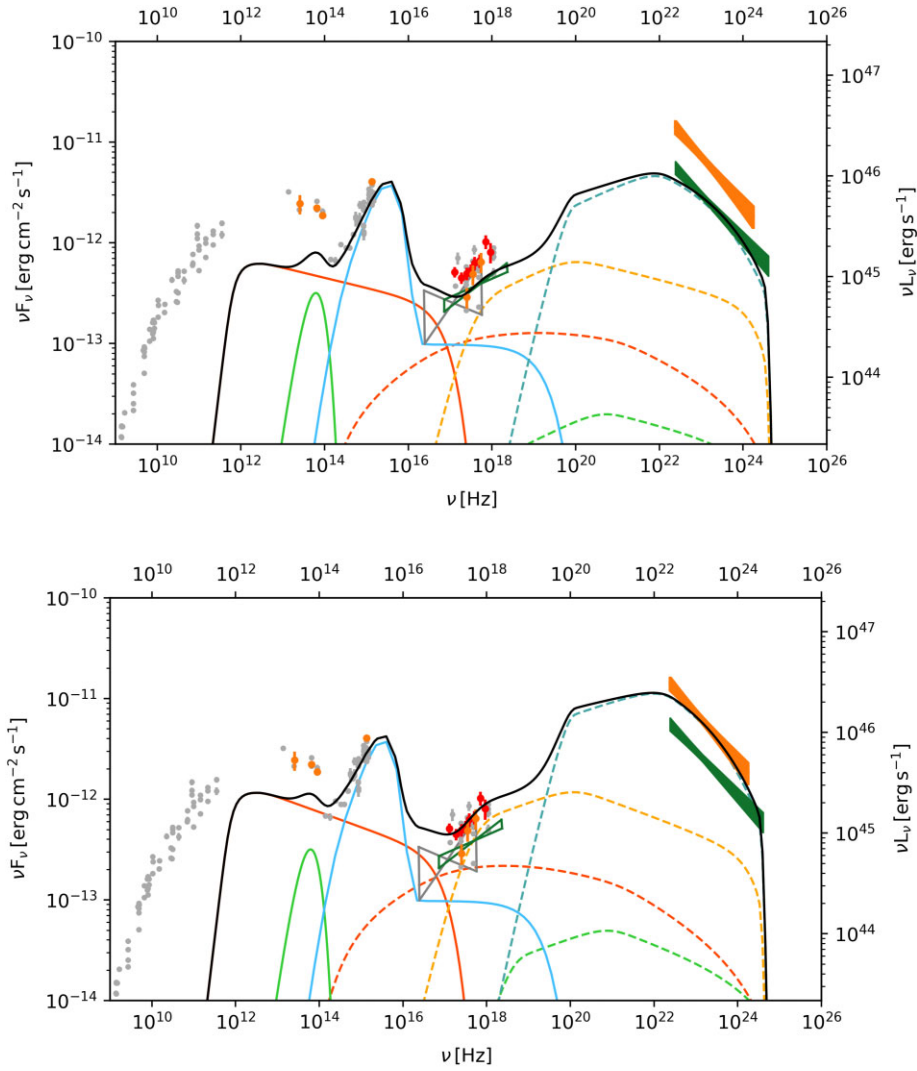
Figure 3. Disc&BLR-dominated scenario for B2 0954+25A. The description of the model components and the data is the same as in Fig. 1.

Table 7. Quasi-simultaneous observations of B2 0954+25A.

Instrument	Time period	MJD
Low state		
Fermi-LAT	2008–2011 (3FGL)	-
Chandra	2009 January 20	54 851
High state		
Fermi-LAT	2010 January–July	55 200–55 400
Swift (UVOT & XRT)	2010 June 15	55 362
WISE	2010 May 7–9	55 323–55 325

2021), as discussed in Section 6.1. The resulting Eddington ratio, $l_{Edd} \sim 0.60$, is relatively high, as in the case of 1H 0323+342.

As for the previous sources, intermediate and the flaring states of B2 0954+25A were modelled in a disc&BLR-IC scenario where the blob is below the BLR and in a torus-IC scenario where the emission region is at the outermost edge of the BLR. The results of the broadband modelling of the two activity states for B2 0954+25A are shown in Fig. 3 and C3 in the BLR- and torus-dominated scenarios, respectively, and the corresponding parameters are given in Table 8.

No change of γ-ray slope being observed between the two states in the case of B2 0954+25A, the electron energy distribution remains unchanged (n_2 index is kept almost constant).

In the disc&BLR-dominated case, both the average and flaring states can be reproduced by a stationary region, with a constant radius of the blob, located at a distance $R_\gamma = 2.1 \times 10^3$ R$_G$ from the BH. Enhanced γ-ray emission is obtained with a more relativistic and denser emitting region (higher electron number density n_e and larger bulk Lorentz factor value). Slight changes in indices and break energy of the particle distribution were made for more accuracy of the fit. The X-ray to γ-ray domain is reproduced by EIC processes (Fig. 3). IC scattering of the BLR photons by the relativistic electrons of the blob is responsible for the observed HE spectrum and the X-ray flux is mainly due to IC scattering of the disc photons. A combination of direct emission from the hot corona and SSC provides a small contribution to the soft X-ray part of the SED, compared to the dominant disc-IC emission.

Contrary to the disc&BLR solutions, in the torus-dominated scenario, where the HE spectrum is due to the IC scattering of the photons from the torus by the relativistic electrons of the emitting region (Fig. C3), electron Lorentz factor values become much larger compared to the disc&BLR solutions, causing a shift in the SED

Table 8. Model parameters for the different scenarios considered for B2 0954+25A. The description of the model input and model-derived parameters is the same as in Table 4.

Source description				
z		0.712		
θ (°)		3		
$M_{BH}[M_\odot]$		1.5×10^8		
R_G [cm]		2.22×10^{13}		
L_{Disc} [erg s^{-1}]		1.13×10^{46}		
l_{Edd}		0.60		
$\dot{m}$ [M$_\odot$ yr^{-1}]		2.39		

Scenario	Disc & BLR		Torus	
State	Average	Flare	Average	Flare
δ	13	15	10	12
K [1 cm^{-3}]	3×10^6	5×10^6	8×10^5	2.5×10^6
R_{src} [cm]	4.96×10^{15}	4.97×10^{15}	5.49×10^{16}	3.77×10^{16}
B [G]	2.4	2.4	0.27	0.30
n_1	2.6	2.7	2.6	2.6
n_2	3.2	3.3	3.75	3.8
γ_{min}	10	10	500	500
γ_b	150	180	680	530
γ_{max}	3×10^4	3×10^4	5×10^4	5×10^4
T_{IR} [K]	1300	1300	1300	1300
τ_{IR}	0.05	0.05	0.20	0.20
α_X	1.0	1.0	1.0	1.0
τ_X	0.10	0.10	0.25	0.25
R_γ [R$_G$]	2.1×10^3	2.1×10^3	7.5×10^4	7.5×10^4
τ_{BLR}	0.30	0.30	1×10^{-4}	1×10^{-4}
R_{in}^{BLR} [R$_G$]	2.5×10^4	2.5×10^4	2.5×10^4	2.5×10^4
u_e/u_b	4.09	4.84	4.14	8.22
n_e [1 cm^{-3}]	4.77×10^4	5.96×10^4	18.10	46.27
u_e [erg cm^{-3}]	9.37×10^{-1}	1.11	1.20×10^{-2}	2.94×10^{-2}
$P_{jet,tot}$ [erg s^{-1}]	2.06×10^{46}	3.98×10^{46}	2.41×10^{45}	4.62×10^{45}

towards higher energies and the non-thermal SSC emission process to account for the X-ray flux. The hot corona contributes to the observed X-ray flux in the torus-dominated case, especially in the soft X-ray band (with enhanced jet emission in the high state, Fig. C3).

In the case of B2 0954+25A, infrared and sub-mm data are clearly underestimated by both disc&BLR and torus-dominated solutions, as opposed to other sources for which the torus-dominated case fills the gap between the modelled synchrotron component and the archival radio-IR data, due to smaller particle densities at larger distances from the BH. It may be that B2 0954+25A requires a strong extended jet, peaking at quite high frequency, to explain the observed radio emission, which makes B2 0954+25A very similar to Ap Librae (Hervet, Boisson & Sol 2015).

Both BLR- and torus-dominated scenarios seem acceptable in the case of B2 0954+25A. However, the disc&BLR solution could be preferred over the torus-dominated case, given the fact that it produces a more energetic jet, in accordance with the FSRQ properties of the source (see Section 7.3).

7 DISCUSSION

7.1 Emission region and mechanism

In our scenarios, the transition from quiescent to flaring states is in general explained by a more relativistic and denser blob in the high state, with larger energy densities of the particle population and

hence larger total jet powers, whereas the parameters describing the environment of the emitting region remain constant. As our solutions indicate an unchanging distance between emission region and BH for the low and flaring states, the observed variability may be explained by an enhanced plasma flow through a stationary shock region (Marscher 2013) or a shock–shock interaction between a moving and a stationary shock (Fichet de Clairfontaine et al. 2021).

This scenario is supported by recent high-resolution VLBA observations of the $\sim(1-100)$ pc scale jet of 1H 0323+342, which revealed the existence of quasi-stationary collimation and acceleration zones in the jet (Hada et al. 2018). Although the limited resolution of the distance scale in that study does not allow us to strictly link their observations to our models, which assume emitting blobs in the sub-pc range, similar structures could exist in regions closer to the BH and be responsible for the acceleration of particles and observed HE emission. A similar mechanism was suggested, for example, for the FSRQ PKS 1510-089 during flares in 2009 (Marscher et al. 2010), where a plasma knot ejected with superluminal velocity was thought to progress in an acceleration and collimation zone of the jet, then passed through a standing shock and led to the γ-ray flare (see also Orienti et al. 2013).

If the parameters of the flare emission region were interpreted as a moving plasma blob, instead of enhanced emission from a stationary region, the emitting blob would be traversing the broad-line region in a few tens of days in the blob frame. In the observer frame, this

would correspond to only a few days, less than the duration of the flaring states. It would be difficult to see how such a scenario could describe the observed duration of the flux variability.

For all three sources, the Lorentz factors of the particles range from $\gamma_{min} \sim 10$ to $\gamma_{max} \lesssim 10^4$ in the disc&BLR-dominated case and the break occurs close to the minimum value, with $\gamma_b \sim 10^2$. In the torus-dominated scenario, the range of electron Lorentz factors is shifted towards higher energies, with γ_{min} values starting at 500 and slightly larger γ_{max} too, compared to the BLR-dominated case. As a consequence, the components responsible for the X-ray emission become entirely non-thermal (SSC + corona) in the torus-dominated case, compared to disc&BLR (where a combination of disc-IC and direct emission from the corona is used to reproduce the X-ray flux).

When estimating the Lorentz factors at which the radiative cooling break would be expected for the different scenarios and states against γ_b applying the usual estimate (Inoue & Takahara 1996), one finds coherent values only for the low state of 1H 0323+342. For all other cases, the radiative cooling break would occur well below the γ_b values derived from modelling, implying that the electron population should already be cooled below γ_b and that γ_b cannot be ascribed to radiative cooling, but possibly to particle escape, to an intrinsic feature of the acceleration process, or it could reflect effects from an inhomogeneous emission region which is parameterized with a simple homogeneous model. If the particle distribution below γ_b is already cooled, this would require a very hard particle injection spectrum with an index $\ll 2$. A possibility may be given by the re-acceleration of an already relativistic particle population, as may be expected, for example, in a shock–shock interaction (Zech & Lemoine 2021).

All our solutions are out of equipartition between electron and magnetic energy densities $u_e/u_B \sim 1$ by a factor of a few and up to an order of magnitude, as is not unusual in standard one-zone blazar emission models. To achieve equipartition in our scenarios would require either a large number of particles or unrealistically high disc-reprocessing factors due to the strong Compton dominance. High activity states are farther away from equipartition, which is not necessarily unexpected given the violent and short-term characteristic of the flares. A plasma with a low magnetization, dominated by the particle energy density, as indicated by our scenarios, is also a requirement for efficient shock acceleration.

7.2 Disc and BLR versus torus scenario

We derived the total jet luminosities from the results of the broad-band SED modelling of all sources from our sample, for both scenarios and for all considered epochs, by computing the different contributions to the total jet power using $P_i = 2\pi R^2 c \Gamma^2 U_i'$. Here the primed quantity is the energy density in the co-moving frame and the index refers to the various contributions: magnetic field, radiation, relativistic electrons, and cold protons[18] and the factor 2 is for a two-sided jet. The values are reported in Table 9, showing that cold protons and radiation account for the bulk of the total jet power and that the power carried by relativistic electrons is the second-most important contribution, while the magnetic flux is the least important contribution. Given the observed large Compton dominance, EIC components (EIC-BLR and EIC-Torus, in the case of BLR- and torus-dominated scenario, respectively) account almost entirely for the total radiative power for each solution, as shown by Table D1, as can be seen in the SEDs too.

---

[18]assuming one cold proton per emitting electron

Large (external-)Compton dominance of γ-NLS1 galaxies is certainly one of the most visible similarities with FSRQs. They also share low values of the break energy γ_b of the electron distribution compared to high-frequency peaked BL Lac objects.

As expected, each source and considered scenario for the EIC scattering requires much larger jet powers for flares than for quiescent states. Interestingly, the disc&BLR-dominated scenarios require significantly larger jet powers compared to the case where the torus dominates the EC radiation, except for 1H 0323+342, for which the results are similar.

We found an increasing radiative efficiency, $\eta_{rad} = P_{rad}/P_{tot}$, between the low and high states for 1H 0323+342 and PMN J0948+0022, as seen by Paliya & Stalin (2016) for another γ-NLS1, PKS 1502+036, during a GeV flare, but with a more significant difference. As regards B2 0954+25A, η_{rad} remains nearly constant between two states for a given scenario (cf. Table 9). The torus-dominated scenario for all sources and particularly for PMN J0948+0022 and B2 0954+25A requires a very large radiative efficiency, between 0.5 and 0.9 for the high states, rendering this scenario less plausible. The radiative efficiency of relativistic jets is generally assumed to be around 10 per cent, as is shown for example by Ghisellini et al. (2014) for a large sample of different types of blazars. A much larger efficiency would result in jets rapidly dissipating their energy and being unable to account for the observed radio lobes and extended emission. The latter is also seen in the SEDs of the sources we consider here, so similar arguments should apply to NLS1s.

The jet emission is much lower in the X-ray band in this scenario than in the disc&BLR one, and, in turn, the luminosity of the hot corona needs to be quite high, much over the 10 per cent usually expected. Another reason to disfavour this scenario.

Apart from energetic considerations, the torus-dominated scenario is also problematic in terms of the size of the emission region, which exceeds by roughly an order of magnitude the limit derived from observed variability time-scales for 1H 0323+342 and PMN J0948+0022.

Given the degeneracy of the standard one-zone model, the values of the parameters used in the models presented above may not be unique in providing a reasonable representation of radio to γ-ray SED. However, lower Doppler factors are not expected as large-electron Lorentz factors are required to produce the strong EIC dominance of the SED. Radio observations showing strong core-dominated jet emission and sometimes superluminal components favour small viewing angles and large Lorentz factors too. Smaller bulk Lorentz factors would allow larger blob radii of the emitting region, located farther away from the central BH than in our cases, which would be at odds with the observed short variability time-scales. Also to keep the synchrotron component below the limits and, at the same time, reproduce the powerful high-energy component, the magnetic field must be kept to relatively low values.

7.3 Jet powers and the nature of γ-NLS1s

The left panel of Fig. 4 represents the total jet powers estimated from SED modelling of different sources and states, as a function of the disc luminosity, for the disc& BLR-dominated scenario (see Fig. C4 for the torus-dominated scenario).

The increase of total jet powers with accretion luminosities is expected, if one assumes that the disc feeds the jet or that both depend on the BH mass and spin. Our preferred solutions for B2 0954+25A and PMN J0948+0022 have jet powers that are up to an order of magnitude larger than the disc luminosity, as was also the case for

Table 9. Physical quantities derived, assuming a two-sided jet, from the modelling of the sources. All quantities are given in units of *erg/s*. Different contributions to the total jet power $P_{\text{tot, jet}}$: Poynting flux power (P_B), total radiative power P_{rad}, the power carried out by relativistic electrons (P_e), and cold protons $P_{p,\text{cold}}$. η_{rad} defined as $P_{\text{rad}}/P_{\text{jet, tot}}$ refers to the radiative efficiency.

Source	Scenario	State	$\log P_e$	$\log P_B$	$\log P_{\text{rad}}$	$\log P_{p,\text{cold}}$	$\log P_{\text{tot, jet}}$	η_{rad}
1H 0323+342	Disc-BLR	Low	43.20	42.21	43.80	44.48	44.58	0.17
		Intermediate	43.32	42.21	43.97	44.58	44.70	0.19
		High	43.78	42.31	44.65	44.94	45.15	0.32
	Torus	Low	43.66	42.62	43.85	44.08	44.38	0.30
		Intermediate	43.62	42.63	43.91	44.00	44.36	0.36
		High	44.38	42.95	44.91	44.75	45.22	0.50
PMN J0948+0022	Disc-BLR	Intermediate	44.67	43.42	46.04	46.48	46.62	0.26
		High	45.08	43.43	46.62	46.85	47.05	0.37
	Torus	Intermediate	44.60	43.89	45.82	44.99	45.91	0.82
		High	44.93	43.64	46.46	45.28	46.50	0.91
B2 0954+25A	Disc-BLR	Low	44.39	43.78	45.14	46.28	46.31	0.07
		High	44.65	43.96	45.52	46.56	46.60	0.08
	Torus	Low	44.30	43.69	45.23	44.66	45.38	0.71
		High	44.56	43.64	45.53	44.93	45.67	0.73
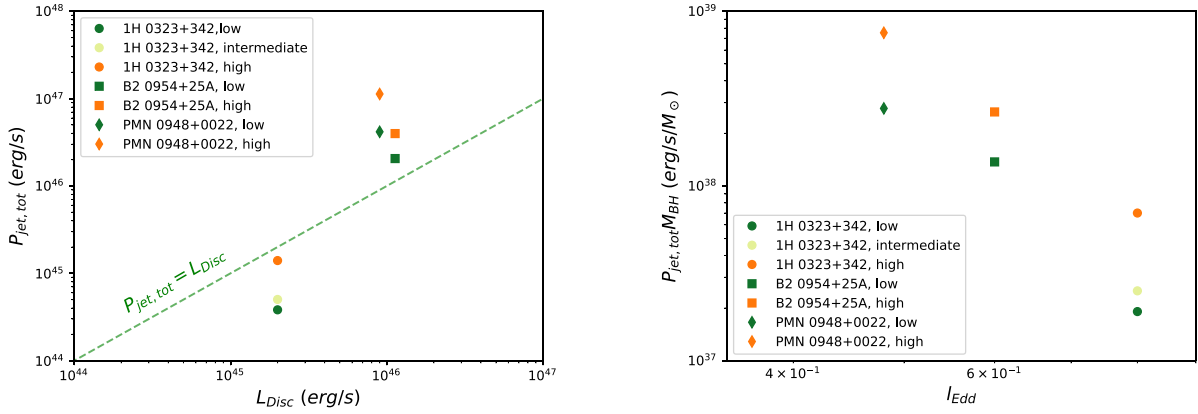
Figure 4. Total jet power versus disc luminosity (left panel) and total jet power corrected for BH mass versus Eddington ratio (right panel) for the disc & BLR-dominated scenario.

PKS J1222 + 0413, a FSRQ tentatively reclassified as a NLSy1 (Kynoch et al. (2019)). Strong dominance of the jet power over the disc luminosity, as seen here, was reported by Ghisellini et al. (2014) for different types of blazars. On the other hand, Paliya et al. (2016) showed that radio-loud NLS1s, including some γ-ray emitters, are characterized by a different trend in the $P_{\text{jet, tot}}$ versus L_{Disc} diagram and that their jet powers are in most cases below the disc luminosity, indicative of higher accretion rates, radiatively efficient discs and relatively low power jets.

In this respect, 1H 0323+342, with a jet power below the disc luminosity, is more typical of the NLS1 population than the other two sources. 1H 0323+342 has the least powerful jet and harbours the least massive BH of the three sources (one order of magnitude below those of B2 0954+25A and PMN J0948+0022).

The results obtained from the present multi-epoch study of the SEDs suggest that 1H 0323+342 remains moderately powerful, regardless of the activity state and adopted scenario.

We find that the jet powers derived from the SED modelling are systematically larger (by almost an order of magnitude) than the estimates provided by Foschini et al. (2015), deduced from the radio core measurements at 15 GHz (see Foschini 2014) ($\log(P_{\text{jet, tot}}) = 43.60$ for 1H 0323+342 and 45.38 for PMN J0948+0022). The statistical relations used to estimate the jet powers from the radio data are based

on a unified view of the astrophysical jets, inducing large associated uncertainties, while jet power estimates from SED modelling are obtained separately for each particular source and epoch.

For 1H 0323+342, when comparing the jet power $log(P_{\text{jet}}) = 44.58$ of the low state in our disc and BLR-dominated scenario to the same *Fermi*-LAT state modelled by Kynoch et al. (2018), we find a result that is larger by less than a factor of 3 with $log(P_{\text{jet}}) = 45.01$. To model the different activity states with a single zone, the photon field from the accretion disc is not sufficient, so we have to place the emission region farther away from disc than Kynoch et al. (2018), leading to a larger jet power. Zhang et al. (2020) have also published jet power estimates from radiative models for a range of activity states of the source, yielding a similar range of values (8×10^{43} to 3×10^{44} erg s^{-1}) to ours (8×10^{43} to 5×10^{44} erg s^{-1}) for the jet power excluding the hadronic contribution. While the overall jet powers are very similar, their solutions present a higher magnetic contribution than ours. D'Ammando et al. (2015) do not provide P_{jet} for their solution, but we can compare the values of the individual components. Our P_e in the BLR-dominated scenario ($\sim 4 \times 10^{44}$ erg s^{-1}) is similar to their value (5.48×10^{44} erg s^{-1}), while P_B and $P_{p,\text{cold}}$ are, respectively, smaller and larger by an order of magnitude.

Comparing our preferred disc&BLR-dominated scenario to the result from Paliya et al. (2019) for the intermediate state of PMN J0948+0022, our jet power is smaller by a factor of 3 ($log(P_{jet})$ = 46.62 versus 47.11), with a considerably smaller contribution from the magnetic field. In our model, the location of the emission region is closer to the central BH and the disc luminosity is higher, which should result in a higher contribution from the EC-disc component and reduce the jet power requirement. An estimate for the jet power for the high state of this source is given again by Zhang et al. (2020), at about a factor 10 smaller than our result. This large difference seems mainly due to a very different shape of the high-energy emission bump, which is much broader in our case.

For B2 0954+25A, only an estimate for a state similar to our low state was found in the literature (Calderone et al. 2012), yielding a very similar jet power to our result, both about 1.5×10^{45} erg/s, but again with a significantly larger magnetic contribution than in our scenario. This is due to a higher magnetic field in the emission region of the model by Calderone et al. (2012), which assumes also a larger distance from the central BH.

Given the large number of free parameters in multi-component EIC models, it is of course difficult to draw general conclusions from these comparisons. The limited observational constraints on the synchrotron emission from the compact blob and the different possible combinations of the EIC contributions to the high-energy component leave, for example, a large range of possible locations of the emission region or strength of the magnetic field.

To verify among our sources whether γ-NLS1 host intrinsically lower power jets or are rather low-mass analogues of blazars, we normalized the jet powers by the black-hole masses (cf. right panel of Fig. 4 and C4). In the disc&BLR-dominated scenario, 1H 0323+342 has the largest Eddington ratio and lowest jet power, even after scaling it by the BH mass, for both low and high states, which supports the conclusions by Kynoch et al. (2018) about its intrinsically low power jet. The other two sources have comparable jet powers after scaling, both at an order of magnitude higher level than 1H 0323+342. These conclusions would not hold for the disfavoured torus-dominated scenario.

Kynoch et al. (2018) demonstrated that 1H 0323+342 cannot be a 'mini' version of FSRQs since the scaling of the FSRQ model to lower BH masses yields larger jet power than the one derived, despite the similarities of its SED properties with the FSRQ class. Similar conclusions were drawn by Abdo et al. (2009a) and Paliya et al. (2014) when comparing with PMN J0948+0022, which in our preferred solution does not differ significantly from the intermediate source B2 0954+25A in terms of scaled jet power.

At the same time, the violent change of the jet powers between low and high states, which is visible from Fig. 4 particularly for 1H 0323+342 and PMN J0948+0022, reflects that these sources are capable of transiting from a low power regime to a blazar-like phase, accounting for their variable spectral features.

The double Seyfert-blazar nature of γ-NLS1s is also supported by their X-ray properties. γ-NLS1s have different X-ray signatures from NLS1 galaxies and are more similar to FSRQs, since they are dominated by the emission from the jet in this frequency range (e.g. Paliya et al. 2019; D'Ammando 2020a). The results of the modelling of our low states show that X-ray data are mainly reproduced by the direct emission from the corona, as also observed for NLS1 galaxies, whereas in the high state non-thermal emission from the jet becomes predominant.

In addition, *Fermi* analysis of γ-NLS1 galaxies performed by Paliya et al. (2015) reported steeper indices of the HE spectra for these sources, compared to generally harder spectra of blazars (see Paliya et al. 2019), which was interpreted as one of the reasons explaining

only few detections of γ-NLS1 in HE. However, the flaring states modelled in the present study show a perhaps more blazar-like behaviour with quite hard HE spectra for PMN J0948+0022 and 1H 0323+342, which is suppressed by the analysis of long-term averaged states.

γ-NLS1 galaxies have not been detected in the VHE band by the existing Cherenkov telescopes. D'Ammando et al. (2015) reported no significant γ-ray signal from PMN J0948+0022 observations by VERITAS following the most powerful flare of PMN J0948+0022 detected by *Fermi*-LAT at the end of 2012. Extrapolation to the VHE band of the LAT measured energy spectrum averaged over the active phase of the flare indeed falls below the VERITAS sensitivity in 5 hr of observation. The probability of the detection by the next generation of *Cherenkov* telescopes, the upcoming CTA project, of the most promising sources of this class was investigated by Romano et al. (2020). According to their results, the vast majority of known γ-NLS1 would remain undetected, even with the sensitivity of the CTA. PMN J0948+0022, if in a flaring state and within some conditions (source located below the BLR, for a specific model of the BLR, see the paper for more details) is one of the three that could be detectable.

8 CONCLUSIONS AND OUTLOOK

We have investigated the main physical properties of two γ-NLS1 galaxies and one intermediate object between FSRQ and γ-NLS1 through the broad-band SED modelling of different activity states, in order to investigate the origin of their γ-ray flares. We analysed their spectral properties, and assessed the energetics of their jets, at the different considered epochs.

Our main conclusions are as follows:

(i) The overall SEDs of the three sources can be explained with a compact stationary emission region inside the jet, a contribution from the BLR and dust torus, a standard optically thick, geometrically thin emission disc and a corona. The dominant high-energy emission is explained by the EIC processes dominated either by photon fields from the disc and BLR or from the torus, depending on the assumed distance of the emission region. An additional emission from the extended jet would be needed to fully account for the radio emission.

(ii) The direct emission from the corona contributes to the X-ray mostly during low/intermediate states in γ-NLS1 galaxies, whereas during flaring episodes, the jet emission contributes the most in this frequency band. This leads to a changing character of the SED – resembling more the emission from Seyfert-1s in the low states and that of blazars in the high states.

(iii) The scenarios in which EIC emission is dominated by photon fields from the disc and BLR are preferred for all three sources due to the large radiative efficiency ($\gg$10 %) for the jet emission that would be required in the torus-dominated scenarios.

(iv) The transition between low, intermediate, and high activity states in γ-rays is explained by changes in the jet emission region only, with a denser, and more relativistic 'blob' with a harder electron spectrum in the high states. The parameters describing the surrounding environment of the blob are kept mostly unchanged.

(v) A physical scenario to account for the flaring states with a stationary source and the energy distribution resulting from our models could be given by the interaction of a moving and a standing shock in which relativistic particles are re-accelerated.

(vi) While the deduced jet power for the preferred disc&BLR-dominated scenario is comparable between the NLS1 PMN J0948+0022 and the FSRQ/intermediate object B2 0954+25A, the other NLS1 1H 0323+342 exhibits a significantly lower jet power, even when scaled to the BH mass.

DATA AVAILABILITY

The data analysis results presented in this paper are available upon request to the authors.

REFERENCES

Abazajian K. N. et al., 2009, ApJS, 182, 543
Abdo A. A. et al., 2009a, ApJ, 699, 976
Abdo A. A. et al., 2009b, ApJ, 707, 727
Abdo A. A. et al., 2009c, ApJ, 707, L142
Abdollahi S. et al., 2020, ApJS, 247, 33
Abdollahi S., 2017, ApJ, 846, 34
Acero F. et al., 2015, ApJS, 218, 23
Adelman-McCarthy J. K. et al., 2006, ApJS, 162, 38
Angelakis E. et al., 2015, A&A, 575, A55
Arrieta-Lobo M., Boisson C., Zech A., 2017, Front. Astron. Space Sci., 4, 56
Baghmanyan V., Sahakyan N., 2018, Int. J. Mod. Phys. D, 27, 1844001
Bentz M. C. et al., 2013, ApJ, 767, 149
Bhattacharyya S., Bhatt H., Bhatt N., Singh K. K., 2014, MNRAS, 440, 106
Boller T., Brandt W. N., Fink H., 1996, A&A, 305, 53
Boroson T. A., Green R. F., 1992, ApJS, 80, 109
Breeveld A. A. et al., 2010, MNRAS, 406, 1687
Burbidge E. M., Strittmatter P. A., 1972, ApJ, 174, L57
Calderone G., Foschini L., Ghisellini G., Colpi M., Maraschi L., Tavecchio F., Decarli R., Tagliaferri G., 2011, MNRAS, 413, 2365
Calderone G., Ghisellini G., Colpi M., Dotti M., 2012, MNRAS, 424, 3081
Calderone G., Ghisellini G., Colpi M., Dotti M., 2013, MNRAS, 431, 210
Cardelli J. A., Clayton G. C., Mathis J. S., 1989, ApJ, 345, 245
Cash W., 1979, ApJ, 228, 939
Cerruti M., Dermer C. D., Lott B., Boisson C., Zech A., 2013, ApJ, 771, L4
Chiaberge M., Marconi A., 2011, MNRAS, 416, 917
D'Ammando F. et al., 2014, MNRAS, 438, 3521
D'Ammando F. et al., 2015, MNRAS, 446, 2456
D'Ammando F., 2019, Galaxies, 7, 87
D'Ammando F., 2020a, MNRAS, 496, 2213
D'Ammando F., 2020b, MNRAS, 498, 859
Dermer C. D., Cerruti M., Lott B., Boisson C., Zech A., 2014, ApJ, 782, 82
Dermer C. D., Menon G., 2009, High Energy Radiation from Black Holes: Gamma Rays, Cosmic Rays, and Neutrinos. Princeton Univ. Press, Princeton, NJ
Dermer C. D., Schlickeiser R., 1993, ApJ, 416, 458
Dermer C. D., Schlickeiser R., Mastichiadis A., 1992, A&A, 256, L27
Fermi Large Area Telescope Collaboration, 2021, Astron. Telegram, 15110, 1
Fichet de Clairfontaine G., Meliani Z., Zech A., Hervet O., 2021, A&A, 647, A77
Finke J. D., Dermer C. D., 2010, Astrophys. J., 714, L303
Foschini L. et al., 2011, MNRAS, 413, 1671
Foschini L. et al., 2012, A&A, 548, A106
Foschini L. et al., 2015, A&A, 575, A13
Foschini L., 2014, Int. J. Mod. Phys. Conf. Ser., 28, 1460188
Foschini L., 2020, Universe, 6, 126
Foschini L., Maraschi L., Tavecchio F., Ghisellini G., Gliozzi M., Sambruna R., 2009, Adv. Space Res., 43, 889
Franceschini A., Rodighiero G., Vaccari M., 2008, A&A, 487, 837

Fuhrmann L. et al., 2016, Res. Astron. Astrophys., 16, 176
Gehrels N. et al., 2004, ApJ, 611, 1005
Ghisellini G., Tavecchio F., 2009, MNRAS, 397, 985
Ghisellini G., Tavecchio F., Maraschi L., Celotti A., Sbarrato T., 2014, Nature, 515, 376
Giroletti M. et al., 2011, A&A, 528, L11
Goodrich R. W., 1989, ApJ, 342, 224
Hada K. et al., 2018, ApJ, 860, 141
Hervet O., Boisson C., Sol H., 2015, A&A, 578, A69
Homan D. C. et al., 2021, ApJ, 923, 67
Inoue S., Takahara F., 1996, ApJ, 463, 555
Jackson N., Browne I. W. A., 1991, MNRAS, 250, 414
Kaspi S., Maoz D., Netzer H., Peterson B. M., Vestergaard M., Jannuzi B. T., 2005, ApJ, 629, 61
Kellermann K. I. et al., 2004, ApJ, 609, 539
Komossa S., Voges W., Xu D., Mathur S., Adorf H.-M., Lemson G., Duschl W. J., Grupe D., 2006, AJ, 132, 531
Kynoch D. et al., 2018, MNRAS, 475, 404
Kynoch D., Landt H., Ward M. J., Done C., Boisson C., Baloković M., Angelakis E., Myserlis I., 2019, MNRAS, 487, 181
Lähteenmäki A. et al., 2017, A&A, 603, A100
Landt H. et al., 2017, MNRAS, 464, 2565
Lister M. L. et al., 2009, Astron. J., 137, 3718
Lister M. L., Homan D. C., Kellermann K. I., Kovalev Y. Y., Pushkarev A. B., Ros E., Savolainen T., 2021, ApJ, 923, 30
Marscher A. P., 2013, ApJ, 780, 87
Marscher A., 2010, ApJ, 710, L126
Oh K. et al., 2018, ApJS, 235, 4
Orienti M., D'Ammando F., Giroletti M., Dallacasa D., Venturi T., Giovannini G., 2013, EPJ Web Conf., 61, 04009
Osterbrock D. E., Pogge R. W., 1985, ApJ, 297, 166
Paliya V. S., Parker M. L., Fabian A. C., Stalin C. S., 2016, ApJ, 825, 74
Paliya V. S., Parker M. L., Jiang J., Fabian A. C., Brenneman L., Ajello M., Hartmann D., 2019, ApJ, 872, 169
Paliya V. S., Sahayanathan S., Parker M. L., Fabian A. C., Stalin C. S., Anjum A., Pandey S. B., 2014, ApJ, 789, 143
Paliya V. S., Stalin C. S., 2016, ApJ, 820, 52
Paliya V. S., Stalin C. S., Ravikumar C. D., 2015, AJ, 149, 41
Rakshit S., Stalin C. S., Chand H., Zhang X.-G., 2017, ApJS, 229, 39
Romano P., Böttcher M., Foschini L., Boisson C., Vercellone S., Landoni M., 2020, MNRAS, 494, 411
Sahakyan N., Baghmanyan V., Zargaryan D., 2018, A&A, 614, A6
Shakura N. I., Sunyaev R. A., 1973, A&A, 500, 33
Shen Y. et al., 2011, ApJS, 194, 45
Sikora M., Begelman M. C., Rees M. J., 1994, ApJ, 421, 153
Sikora M., Stawarz Ł., Moderski R., Nalewajko K., Madejski G. M., 2009, ApJ, 704, 38
Spergel D. N. et al., 2003, ApJS, 148, 175
Torniainen I., Tornikoski M., Teräsranta H., Aller M. F., Aller H. D., 2005, A&A, 435, 839
Yao S., Yuan W., Komossa S., Grupe D., Fuhrmann L., Liu B., 2015, Astron. J., 150, 23
Yuan W., Zhou H. Y., Komossa S., Dong X. B., Wang T. G., Lu H. L., Bai J. M., 2008, ApJ, 685, 801
Zech A., Lemoine M., 2021, A&A, 654, A96
Zhang J., Zhang H.-M., Gan Y.-Y., Yi T.-F., Wang J.-F., Liang E.-W., 2020, ApJ, 899, 2
Zhou H. et al., 2007, ApJ, 658, L13
Zhou H.-Y., Wang T.-G., Dong X.-B., Zhou Y.-Y., Li C., 2003, ApJ, 584, 147
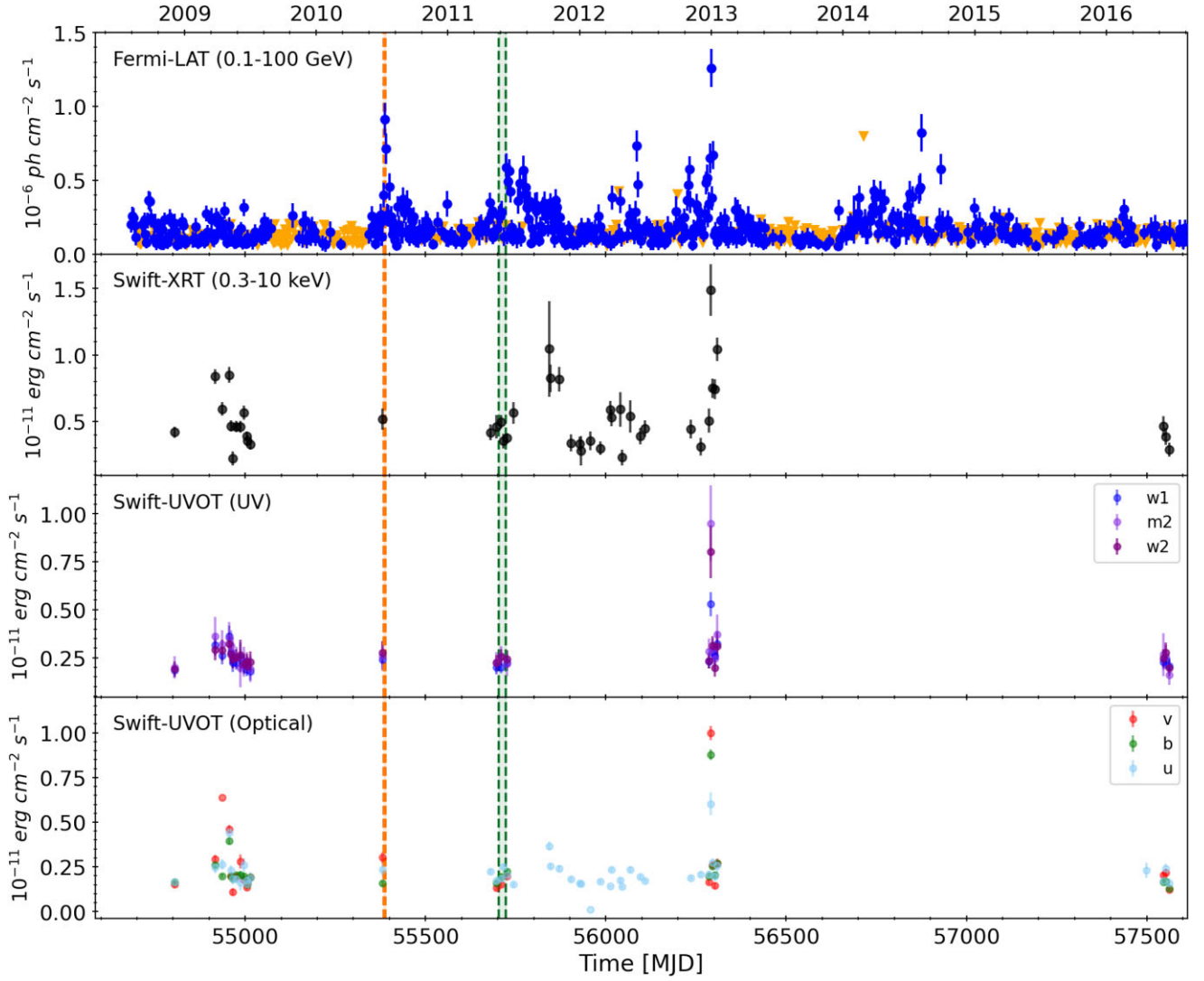
APPENDIX A: MULTI-FREQUENCY LIGHT CURVES

Fermi data are retrieved from *Fermi* light curve repository.[19]

[19] https://fermi.gsfc.nasa.gov/ssc/data/access/lat/LightCurveRepository/
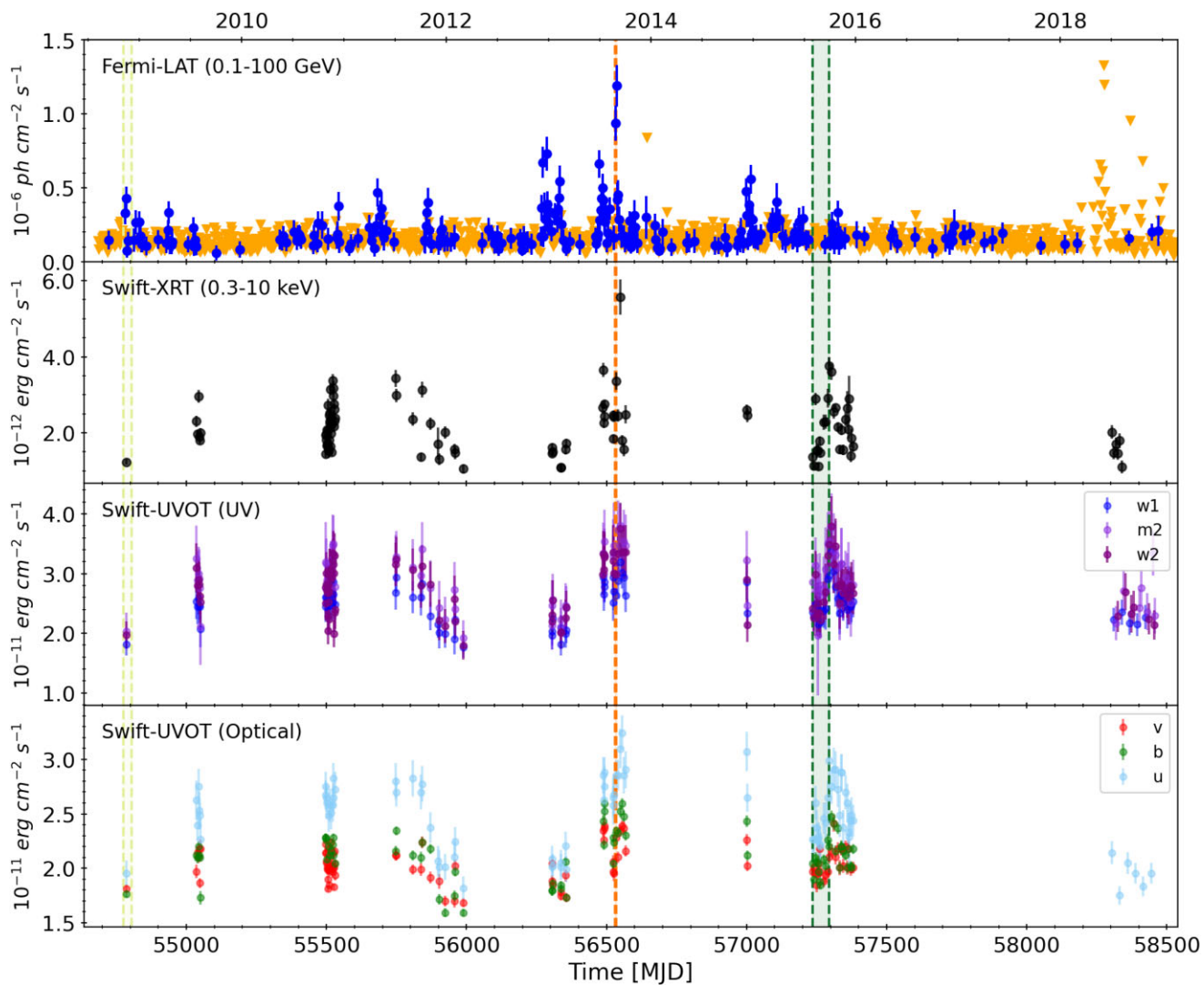
Figure A1. Multifrequency light curves of 1H 0323+342. Upper panel: 3 day binned *Fermi*-LAT light curve, photon flux in the 0.1–100 GeV energy range, in units of 10^{-6} ph cm^{-2} s^{-1}. Middle panel: XRT flux in the 0.3–10 keV energy range, in units of 10^{-11} erg cm^{-2} s^{-1}. Lower panel: UVOT flux in the different optical and UV bands of *Swift*, in units of mJy. *Swift* XRT and UVOT data are retrieved from D'Ammando (2020a). For more visibility, the entire light curves are not shown and they are truncated to focus on the periods of interest.

Figure A2. Multifrequency light curves of PMN J0948+0022. Upper panel: 3 day binned *Fermi*-LAT light curve, photon flux in the 0.1–100 GeV energy range, in units of 10^{-6} ph cm^{-2} s^{-1}. Middle panel: XRT flux in the 0.3–10 keV energy range, in units of 10^{-12} erg cm^{-2} s^{-1} Lower panel: UVOT flux in the different optical and UV bands of *Swift*, in units of mJy. *Swift* XRT and UVOT data are retrieved from D'Ammando ([2020a](#)). For more visibility, the entire light curves are not shown and they are truncated to focus on the periods of interest.
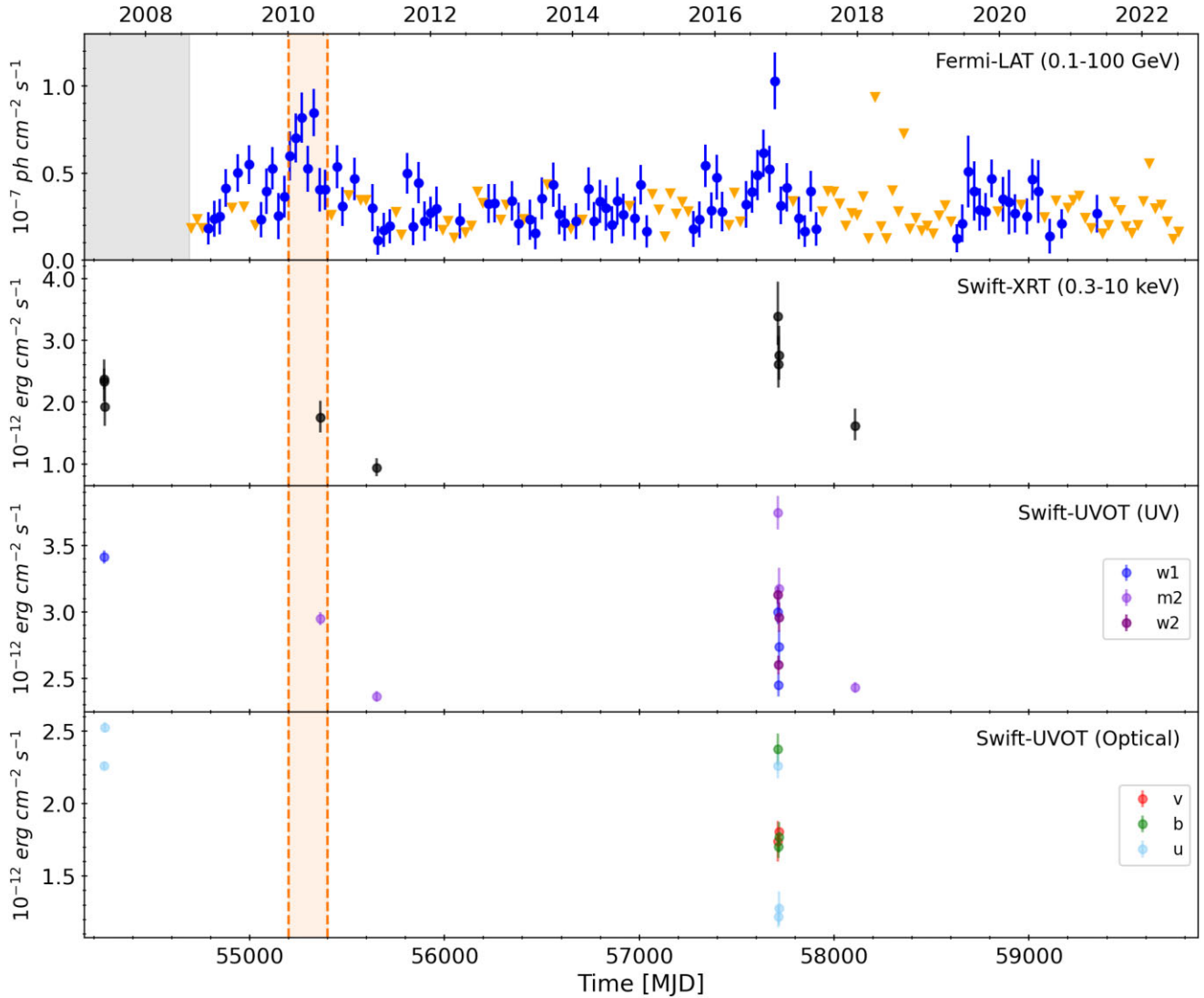
Figure A3. Multifrequency light curves of B2 0954+25A. Upper panel: monthly-binned *Fermi*-LAT light curve, photon flux in the 0.1–100 GeV energy range, in units of 10^{-7} ph cm^{-2} s^{-1}. Middle panel: XRT flux in the 0.3–10 keV energy range, in units of 10^{-12} erg cm^{-2} s^{-1}. Lower panel: UVOT flux in the different optical and UV bands of *Swift*, in units of mJy. The greyed area delimits the period before the start of *Fermi* observations. Note that we only show the flaring state, since the modelled low state refers to the entire 3FGL flux.

APPENDIX B: DATA ANALYSIS

B1 *Fermi*-LAT data

We downloaded LAT data from the *Fermi* Science Support Center archive[20] for the different targets and time periods of interest and considered all photons in a circular region of interest (RoI) of radius $10°$, centred on the source position. A zenith-angle cut of $90°$ was applied. The analysis was done with the *Fermi* ScienceTools software package[21] version v11r5p3, in combination with PASS 8 instrument response functions (event class 128 and event type 3) corresponding to the P8R3_SOURCE_V3 response and the gll_iem_v07.fits and iso_P8R3_SOURCE_V3_v1.txt models for the Galactic and diffuse background, respectively. The source model used include all sources of the 4FGL catalogue (Abdollahi et al. 2020) that fall within $15°$

of the RoI center. A binned likelihood analysis was applied in an iterative way, fixing the spectral shape parameters for 4FGL sources more than $10°$ away to account for event leakage in the RoI due to the large PSF at low energies. In a second step, the sources contributing to less than 5 per cent of the total number of counts in the RoI and/or with significance, derived from test statistic, $TS < 9$ have their parameters frozen. In the end, the only free parameters are those of sources less than $3°$ away from the target, if not frozen in the previous step and the normalizations of the two diffuse background components.

All the uncertainties presented in this paper are statistical only.

B2 *Swift* analysis-B2 0954+25A

The Neil Gehrels *Swift* Observatory (Gehrels et al. 2004) performed only nine observations of B2 0945+25A in 18 years (see Table B1). The hard X-ray flux of this source is below the sensitivity of the BAT instrument for the short exposures of these observations,

[20]https://fermi.gsfc.nasa.gov/cgi-bin/ssc/LAT/LATDataQuery.cgi
[21]https://fermi.gsfc.nasa.gov/ssc/data/analysis/software/

Table B1. Summary of the *Swift*-XRT observations of B2 0954+25A.

Date	MJD start	Obs. ID	Exposure ks	Index	Flux(0.3–10 keV) 10^{-12} erg cm^{-2} s^{-1}
2007 May 31	54251.69	00036325001	2.0	1.69 ± 0.16	2.33 ± 0.36
2007 June 01	54252.03	00036325002	7.6	1.73 ± 0.08	2.37 ± 0.18
2007 June 05	54256.05	00036325003	2.0	1.62 ± 0.20	1.93 ± 0.36
2010 June 15	55362.21	00036325004	2.6	1.76 ± 0.18	1.75 ± 0.27
2011 March 30	55650.26	00036325005	4.8	1.82 ± 0.20	0.94 ± 0.16
2016 November 18	57710.88	00036325006	2.0	1.46 ± 0.16	3.39 ± 0.55
2016 November 22	57714.47	00036325007	2.0	1.52 ± 0.18	2.62 ± 0.45
2016 November 24	57716.20	00036325008	1.9	1.63 ± 0.18	2.76 ± 0.48
2017 December 19	58106.83	00088202001	2.3	1.80 ± 0.20	1.62 ± 0.28

Table B2. Summary of the *Swift*-UVOT observations of B2 0954+25A.

Date	MJD start	Obs. ID	n_{images}	U	B	V	UVW1	UVM2	UVW2
2007 May 31	54251.69	00036325001	5				16.53 ± 0.04		
2007 June 01	54252.03	00036325002	10	17.08 ± 0.04					
2007 June 05	54256.05	00036325003	3	17.01 ± 0.04					
2010 June 15	55362.21	00036325004	1					17.72 ± 0.04	
2011 March 30	55650.26	00036325005	1					16.96 ± 0.04	
2016 November 18	57710.88	00036325006	1	17.17 ± 0.07	18.06 ± 0.09	17.56 ± 0.09	16.94 ± 0.07	16.61 ± 0.07	16.95 ± 0.05
2016 November 22	57714.47	00036325007	1	17.61 ± 0.06	18.27 ± 0.07		17.02 ± 0.06		17.14 ± 0.06
2016 November 24	57716.20	00036325008	2	17.57 ± 0.08	18.19 ± 0.09	18.17 ± 0.20	17.05 ± 0.07	16.75 ± 0.07	17.03 ± 0.06
2017 December 19	58106.83	00088202001	3					16.96 ± 0.05	

also the source is not present in the Swift BAT 105-month hard X-ray catalogue (Oh et al. 2018). We thus only analysed all the X-ray Telescope (XRT, 0.2–10.0 keV) and the Ultraviolet/Optical Telescope (UVOT) available data.

The XRT telescope data were processed with the XRTDAS software package within the HEASoft 6.29c package.[22] Event files were calibrated and cleaned with the default filtering criteria with the xrtpipeline v0.13.6 task. The spectrum was extracted from the summed and cleaned event file with the xselect task. The source extraction region was a 47.2 arcsec radius centred on the source, while background events were extracted from a circular region with radius of 70 arcsec away from the source region and any other source. The ancillary response files were generated with the xrtmkarf task and the latest response matrices available in the *Swift* CALDB were used. As the spectra have a low numbers of photons, before the spectral fitting, the source spectra were grouped with the grppha task to ensure a minimum of 1 count per bin and the fit performed with the Cash statistic (Cash (1979)).

The spectrum of each *Swift*-XRT observation was fitted with a simple power law with the hydrogen column fixed to the Galactic absorption column of 3.47×10^{20} atoms cm^{-2} using the XSPEC
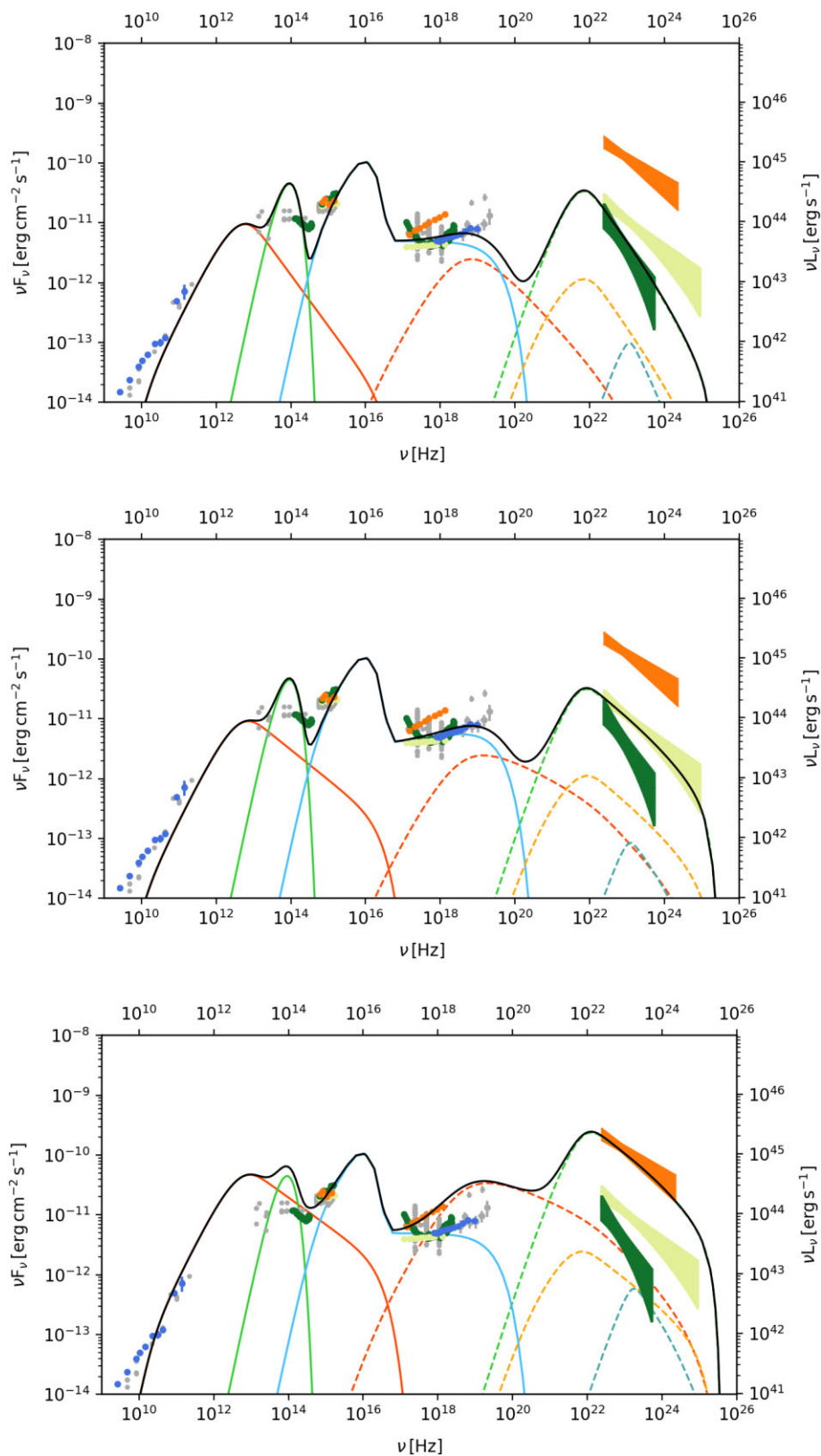
12.9.1 package. The resulting photon index and de-absorbed flux in the 0.3–10 keV energy are given in Table B1.

During the *Swift* pointings, the UVOT instrument observed the source in at least one of its six photometric bands.[23] An aperture photometry analysis was performed. Separate images within a given file were integrated with the uvotimsum task and then analysed by using the uvotsource task. Source counts were extracted from a circular region of 5 arcsec radius centred on the source, while background counts were derived from a 20 arcsec radius region located in a nearby source-free area. The UVOT magnitudes are corrected for Galactic extinction using $E(B - V) = 0.0325$ mag and the extinction laws from Cardelli, Clayton & Mathis (1989) and converted to flux densities using the conversion factors from Breeveld et al. (2010).
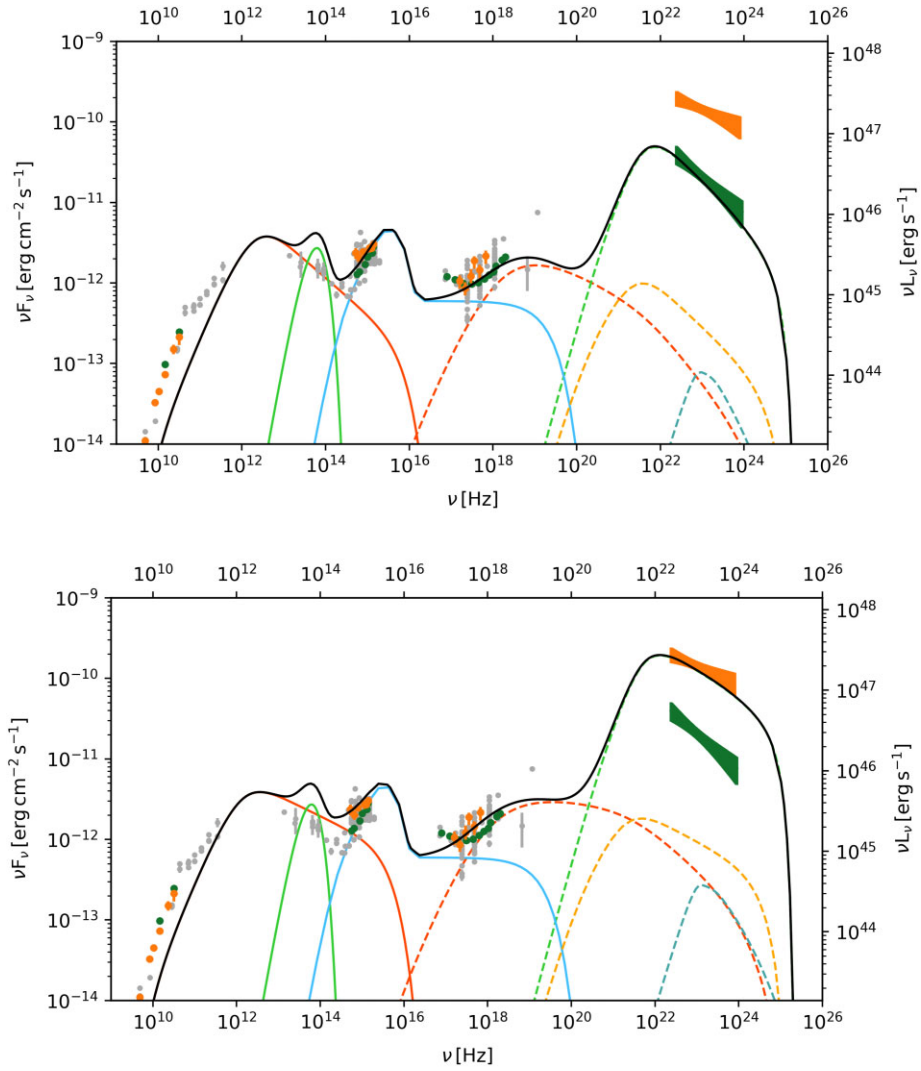
APPENDIX C: TORUS-EIC MODEL RESULTS

---

[22] https://heasarc.gsfc.nasa.gov/docs/software/lheasoft/download.html

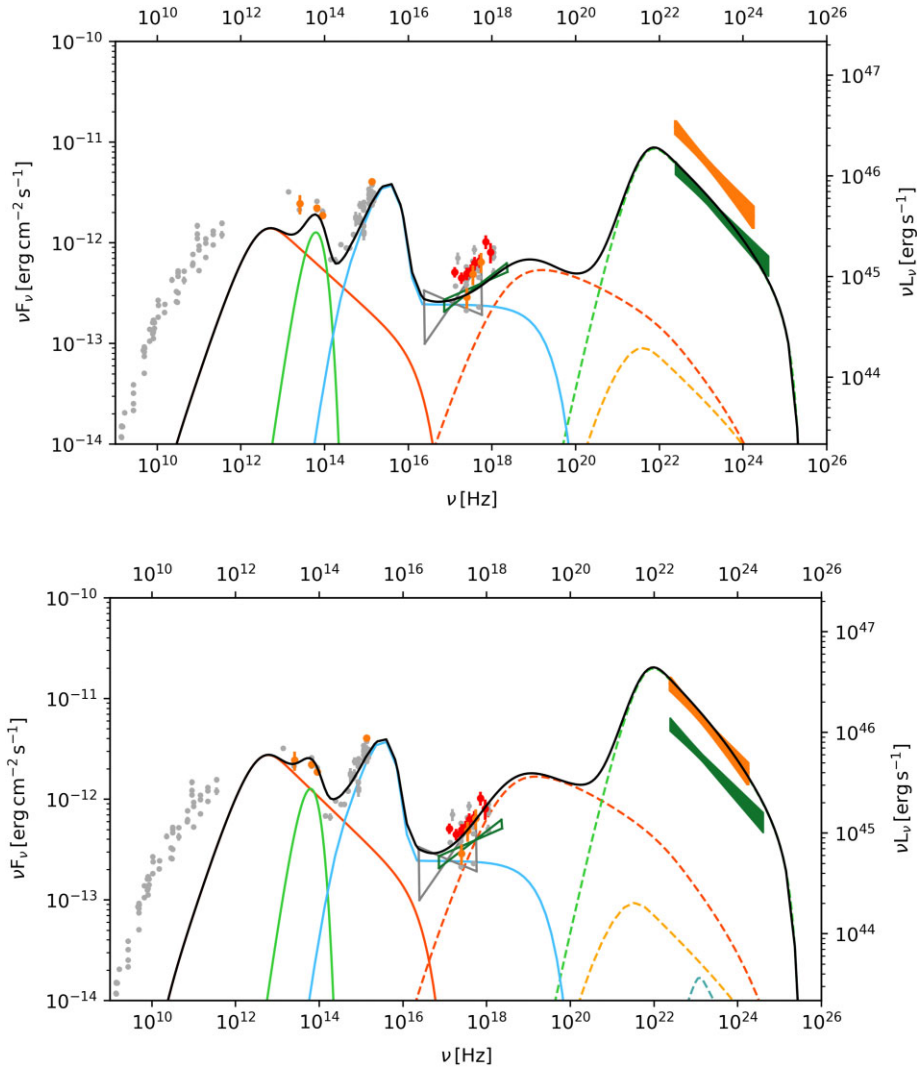[23] V (500–600 nm), B (380–500 nm), U (300–400 nm), UVW1 (220–400 nm), UVM2 (200–280 nm), and UVW2 (180–260 nm)
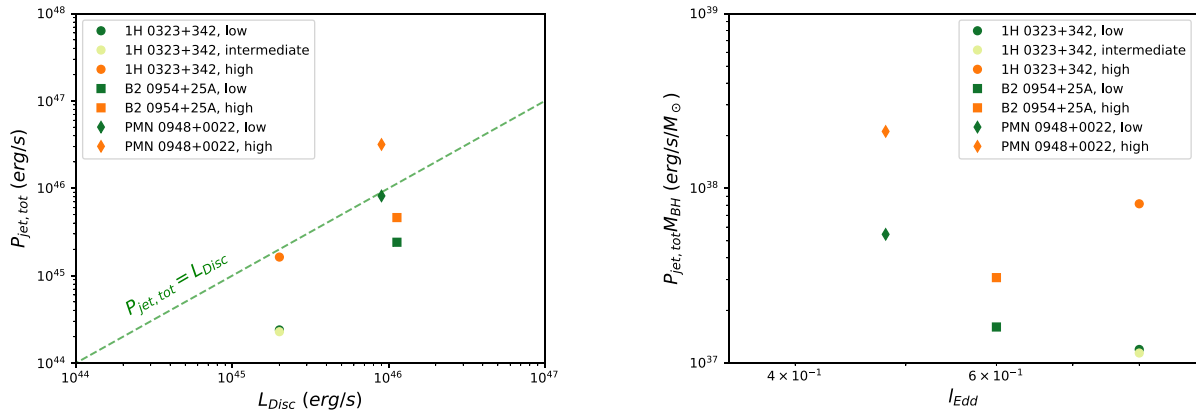
Figure C1. Torus-dominated scenario for 1H 0323+342. The description of the model components and the data is the same as in Fig. 1.

Figure C2. Torus-dominated scenario for PMN J0948+0022. The description of the model components and the data is the same as in Fig. 1.

Figure C3. Torus-dominated scenario for B2 0954+25A. The description of the model components and the data is the same as in Fig. 1.

Figure C4. Total jet power versus disc luminosity (left panel) and total jet power corrected for BH mass versus Eddington ratio (right panel) for torus-dominated scenario.

APPENDIX D: COMPONENTS OF THE RADIATIVE POWER FOR ALL MODELS

Table D1. Different contributions to the total radiative power from synchrotron, SSC, EIC of the disc, torus, and BLR photons.

Source	Scenario	State	Syn	SSC	EIC-disc	EIC-torus	EIC-BLR	$P_{\mathrm{rad},\,tot}$
1H 0323+342	Disc-BLR	Low	3.05×10^{41}	8.04×10^{40}	7.19×10^{42}	6.95×10^{40}	5.57×10^{43}	6.33×10^{43}
		Intermediate	5.05×10^{41}	2.08×10^{41}	1.11×10^{43}	1.08×10^{41}	8.06×10^{43}	9.26×10^{43}
		High	2.73×10^{42}	4.13×10^{42}	3.66×10^{43}	6.99×10^{41}	4.05×10^{44}	4.50×10^{44}
	Torus	Low	1.49×10^{42}	5.38×10^{41}	3.23×10^{41}	6.80×10^{43}	1.23×10^{41}	7.04×10^{43}
		Intermediate	1.77×10^{42}	7.31×10^{41}	3.73×10^{41}	7.84×10^{43}	1.25×10^{41}	8.14×10^{43}
		High	1.01×10^{43}	1.14×10^{43}	9.08×10^{41}	7.94×10^{44}	1.11×10^{42}	8.18×10^{44}
PMN J0948+0022	Disc-BLR	Intermediate	5.41×10^{42}	1.99×10^{42}	6.87×10^{43}	1.33×10^{43}	1.08×10^{46}	1.09×10^{46}
		High	3.02×10^{43}	3.99×10^{43}	5.19×10^{44}	7.56×10^{43}	4.10×10^{46}	4.17×10^{46}
	Torus	Intermediate	5.20×10^{43}	3.47×10^{43}	2.37×10^{43}	6.55×10^{45}	6.34×10^{42}	6.67×10^{45}
		High	5.05×10^{43}	5.85×10^{43}	4.04×10^{43}	2.85×10^{46}	2.18×10^{43}	2.87×10^{46}
B2 0954+25A	Disc-BLR	Low	1.61×10^{43}	5.66×10^{42}	3.87×10^{43}	8.32×10^{42}	1.32×10^{45}	1.39×10^{45}
		High	2.26×10^{43}	7.95×10^{42}	5.69×10^{43}	1.95×10^{43}	3.22×10^{45}	3.33×10^{45}
	Torus	Low	3.05×10^{43}	1.90×10^{43}	3.39×10^{42}	1.64×10^{45}	8.00×10^{41}	1.70×10^{45}
		High	4.35×10^{43}	4.27×10^{43}	2.55×10^{42}	3.26×10^{45}	1.50×10^{43}	3.35×10^{45}

This paper has been typeset from a TEX/LATEX file prepared by the author.